THESIS FOR THE DEGREE OF DOCTOR OF PHILOSOPHY

Microwave FET Modeling and Applications

STATISTICAL MODEL PARAMETER ESTIMATION
POWER AMPLIFIER INTERMODULATION DISTORTION ANALYSIS
FMCW RADAR TRANSCEIVERS

Christian Fager

Submitted to the School of Electrical Engineering,
Chalmers University of Technology, in partial fulfillment of the
requirements for the degree of Doctor of Philosophy

Department of Microtechnology and Nanoscience
Microwave Electronics Laboratory
CHALMERS UNIVERSITY OF TECHNOLOGY
Göteborg, Sweden 2003

Microwave FET Modeling and Applications

CHRISTIAN FAGER
ISBN 91–7291–286–3

Doktorsavhandlingar vid Chalmers Tekniska Högskola
Ny serie 1968
ISSN 0346–718X

Technical report No. 441
ISSN 1651-498X
School of Electrical Engineering
Chalmers University of Technology
SE-412 96 Göteborg
Sweden
Tel. +46 (0)31 772 1000

Printed by Bibliotekets Reproservice
Chalmers University of Technology
Göteborg, Sweden, April 2003

Abstract

This thesis deals with three distinct topics within the areas of modeling, analysis and circuit design with microwave field effect transistors (FETs).

First, the extraction of FET small-signal model parameters is addressed. A method is presented where the model parameter uncertainties are derived from *S*-parameter measurement uncertainties and uncertainties in the parasitic elements. This allows a method to be presented where each model parameter is determined with minimum uncertainty, thus being optimal in a statistical sense. Accurate extractions can thereby be performed independent of the specific device characteristics or bias point.

Thereafter, analysis of intermodulation distortion (IMD) in power amplifiers (PAs) is treated. A new analysis method is described where the large-signal IMD behavior of PAs can be analytically predicted. The method allows the IMD generating mechanisms to be identified, thus providing a tool for tailoring device characteristics for IMD reduction. The method has been used to predict the large-signal IMD behavior of LDMOS and CMOS PA circuits. The IMD prediction capabilities of common large-signal transistor models have been evaluated, which led to modifications to an industry-standard LDMOS model being proposed.

Finally, FMCW radar transceivers are described. A FET transceiver suitable for FMCW radars is presented. The transceiver utilizes the FET simultaneously to amplify the transmitted signals and as a resistive mixer to down-convert the received signal. Therefore, unlike most existing FMCW radar transceivers, the transmitted and received signals do not need to be separated. Since AM noise rejection is important in FMCW radars, a similar balanced FET transceiver is also presented. Compared to the unbalanced transceiver, the AM noise performance is substantially improved. The transceivers' simple topology and the elimination of the need for separation of transmitted and received signals make them suitable for integration in MMIC technology.

Keywords

FET, MESFET, HEMT, LDMOS, CMOS, small-signal, large-signal, model, estimation, extraction, uncertainty, statistical, power amplifier, intermodulation, distortion, FMCW, radar, AM noise

Table of contents

List of appended papers

The thesis is based on the following papers:

[A] C. Fager, P. Linnér, and J. C. Pedro, "Optimal parameter extraction and uncertainty estimation in intrinsic FET small-signal models," *IEEE Transactions on Microwave Theory and Techniques*, vol. 50, pp. 2797-803, Dec. 2002.

[B] C. Fager, K. Andersson, P. Linnér, and H. Zirath "Statistical estimation of intrinsic transistor small-signal model parameters," *Manuscript*.

[C] C. Fager and P. Linner, "A general de-embedding method," *Submitted to IEE Electronics Letters*, Feb. 2003.

[D] C. Fager, J. C. Pedro, N. B. Carvalho, and H. Zirath, "Prediction of IMD in LDMOS transistor amplifiers using a new large-signal model," *IEEE Transactions on Microwave Theory and Techniques*, vol. 50, pp. 2834-42, Dec. 2002.

[E] C. Fager, J. C. Pedro, N. B. Carvalho, H. Zirath, F. Fortes, and M. J. Rosário, "A comprehensive analysis of IMD behavior in RF CMOS power amplifiers," *Submitted to IEEE Journal of Solid-State Circuits*, Jan. 2003.

[F] K. Yhland and C. Fager, "A FET transceiver suitable for FMCW radars," *IEEE Microwave and Guided Wave Letters*, vol. 10, pp. 377-9, Sept. 2000.

[G] C. Fager, K. Yhland, and H. Zirath, "A balanced FET FMCW radar transceiver with improved AM noise performance," *IEEE Transactions on Microwave Theory and Techniques*, vol. 50, pp. 1224-7, Apr. 2002.

Other papers

The following papers are not included due to an overlap in contents or a content which goes beyond the scope of this thesis:

[R1] C. Fager, P. Linnér, and J. C. Pedro, "Uncertainty estimation and optimal extraction of intrinsic FET small-signal model parameters," Proc. IEEE MTT-S International Microwave Symposium, pp. 729-32, 2002.

[R2] J. M. Miranda, C. Fager, H. Zirath, P. Sakalas, S. Munoz, and J. L. Sebastian, "Influence of the calibration kit on the estimation of parasitic effects in HEMT devices at microwave frequencies," *IEEE Transactions on Instrumentation and Measurement*, vol. 51, pp. 650-5, Aug. 2002.

[R3] C. Fager, J. C. Pedro, N. B. Carvalho, and H. Zirath, "Intermodulation distortion behavior in LDMOS transistor amplifiers," Proc. IEEE MTT-S International Microwave Symposium, pp. 131-4, 2002.

[R4] J. Olsson, N. Rorsman, L. Vestling, C. Fager, J. Ankarcrona, H. Zirath, and K.-H. Eklund, "1 W/mm RF power density at 3.2 GHz for a dual-layer RESURF LDMOS transistor," *IEEE Electron Device Letters*, vol. 23, pp. 206-8, Apr. 2002.

[R5] C. Fager, "Characterisation of an FMCW radar transceiver," Department of Microelectronics, Chalmers University of Technology, Göteborg, Research report no.7, 1999.

[R6] D. Weinholt, C. Fager, G. Skatt, and K. Jarl, "Apparatus in a microwave system," Swedish Patent application (No. 0101159-2), Telefonaktiebolaget LM Ericsson AB, 2001.

[R7] C. Fager, L. Landen, and H. Zirath, "High output power, broadband 28-56 GHz MMIC frequency doubler," Proc. IEEE MTT-S International Microwave Symposium, pp. 1589-91, vol. 3, 2000.

[R8] H. Zirath, L. Landen, and C. Fager, "An active millimeter wave MMIC frequency doubler with high spectral purity and low power consumption," Proc. European Gallium Arsenide and Related III-V Compounds Application Symposium (GAAS99), 1999.

[R9] L. Landen, C. Fager, and H. Zirath, "Regenerative GaAs MMIC frequency dividers for 28 and 14 GHz," Proc. 30th European Microwave Conference, vol. 1, pp. 184-6, 2000.

[R10] H. Zirath, C. Fager, M. Garcia, P. Sakalas, L. Landen, and A. Alping, "Analog MMICs for millimeter-wave applications based on a commercial 0.14- mu m pHEMT technology," *IEEE Transactions on Microwave Theory and Techniques*, vol. 49, pp. 2086-92, Nov. 2001.

[R11] M. Garcia and C. Fager, "A design equation for the load resistors that ensure stability for potentially unstable transistors," Proc. SBMO/IEEE MTT-S International Microwave and Optoelectronics Conference, pp. 589-91, 1999.

Abbreviations and notations

Abbreviations

ac	Alternating Current
ACPR	Adjacent Channel Power Ratio
AICC	Automotive Intelligent Cruise Control
AM	Amplitude Modulation
BJT	Bipolar Junction Transistor
BLUE	Best Linear Unbiased Estimator
CAE	Computer Aided Engineering
CMOS	Complementary MOS
dc	Direct Current
DFT	Discrete Fourier Transform
DSB	Double SideBand
FET	Field Effect Transistor
FM	Frequency Modulation
FMCW	Frequency Modulated Continuous Waveform
FOM	Figure Of Merit
HB	Harmonic Balance
HEMT	High Electron Mobility FET
IC	Integrated Circuit
IF	Intermediate Frequency
IIP3	Input 3^{rd} order Intercept Point
IMD	InterModulation Distortion
InP	Indium Phosphide
LDMOS	Laterally Diffused MOS
LRM	Line–Reflect–Match
MESFET	MEtal–Semiconductor FET
MMIC	Monolithic Microwave Integrated Circuit
MOSFET	Metal–Oxide–Semiconductor FET
OIP3	Output 3^{rd} order Intercept Point
PA	Power Amplifier
PWTF	PieceWise Transfer Function
RF	Radio Frequency
RX	Receive
SB	Spectral Balance
TF	Transfer Function
TRL	Thru–Reflect–Line
TX	Transmit
VNA	Vector Network Analyzer
W-CDMA	Wideband Code Division Multiple Access

Notations

C	Capacitance
f	Frequency
I	Current
i_{DS}	Dynamic drain–source current
$I_{DS,bias}$	Drain–source bias current
$I_{DS,dc}$	Gate–source dc current
K	Relative sensitivity
L	Inductance
R	Resistance
S	Scattering parameter
σ	Standard deviation
σ^2	Variance
V	Voltage
v_{DS}	Dynamic drain–source voltage
$V_{DS,bias}$	Drain–source bias voltage
v_{GS}	Dynamic gate–source voltage
$V_{GS,bias}$	Gate–source bias voltage
ω	Angular frequency
Y	Admittance
Z	Impedance

Chapter 1. Introduction

Microwave applications have evolved from low volume customized products to a mass market during the last decade. The largest production volume is associated with mobile communications equipment (< 5 GHz), but large quantities of microwave circuits are also produced for satellite television receivers (10–12 GHz). Microwave and millimeter wave circuits are used in fixed point-to-point as well as point-to-multipoint microwave links (7–40 GHz). These links are mainly used for high capacity transmission within mobile communications networks. The need for high capacity transmission will most likely continue to grow with the implementation of the third- and fourth generation cellular telephone networks. Military and radio astronomy applications still dominate for frequencies above 40 GHz. However, the high demands on transmission capacity will probably open these frequencies to large volume commercial applications in the near future [1].

A short time to market is crucial in commercial large-volume production. This can be achieved with short prototyping turnaround times and first time success for circuit designs. Since large-volume production also requires high circuit yield, manufacturing and modeling uncertainties have to be accounted for at the design stage [2]. Accurate device models and knowledge of the model uncertainties are therefore crucial.

The active device, in most cases a field effect transistor (FET), is usually the most critical part of a microwave circuit design. Although FET models and parameter extraction methods are commonly used, there are no available methods for evaluating the uncertainty in the obtained parameters. This problem is addressed in [Papers A-C] and Chapter 2, which gives a background to these methods.

Transmission capacity and cost is also of primary concern in commercial large-volume products. This demands full utilization of the available spectral bandwidth and the use of inexpensive components. Effective spectral utilization is achieved with complex modulation schemes, which requires low distortion levels of the transmitted signals [3]. Hence, it is necessary with a thorough understanding of the mechanisms distorting the signals in microwave transmitters.

Laterally diffused metal oxide semiconductor (LDMOS) transistors are today used as the most cost-effective components for high power amplification in e.g. cellular base-stations [4, 5], while integrated complementary metal oxide semiconductor (CMOS) amplifiers are used for hand-held transceivers [6-9]. However, a simple explanation for the distortion in power amplifiers (PAs) based on these devices has not been available. [Paper D] and [Paper E] describe such methods. These as well as other methods are discussed in Chapter 3.

Automotive intelligent cruise control (AICC) and collision avoidance radars [10, 11] are potential mass-market products for the 80 GHz frequency range. In order to reduce the cost of production the entire radar transceiver has to be integrated on a single chip. Existing solutions require space consuming off-chip separation of the transmitted and received signals, thus preventing full-scale integration. [Paper F] and [Paper G] present a solution to this problem. Chapter 4 describes this and other existing methods used for low-cost radar transceivers designs.

Chapter 2. Statistical estimation of FET small-signal model parameters

The traditional use of FET small-signal models is for linear circuit analysis. Besides, they also serve as basis for empirical large-signal models and their parameters are used to evaluate FET processing variations.

For metal-semiconductor FETs (MESFETs) and high electron mobility transistors (HEMTs), the small-signal model parameters are usually determined from the direct extraction method, originally proposed by Dambrine *et al.* [12]. Extensions to the original method are reported in [13, 14], and it is now used also for other devices, such as metal-oxide-semiconductor FETs (MOSFETs) [15]. In all cases above, accuracy in the modeled response and extracted model parameters is of primary concern.

Despite this wide range of applications, very little work has been reported on how to determine the uncertainty in the extracted results.

In this chapter, the first section gives an overview of the direct extraction method, and how various sources of uncertainty enter the method. Consequently, the *true* model parameter values can not be determined but only *estimated* with some uncertainty.

Section 2.2 describes a method for estimating the model parameters with minimal uncertainty. A simple *R–C* model example is used to illustrate the method. The uncertainty in the modeled *S*-parameter response is also treated.

This statistical estimation method is in Section 2.3 applied to FET model direct-extraction. Emphasis is on the measurement and parasitic element uncertainties and how they affect the estimation results. Different applications of the obtained results are also presented.

The final Section 2.4 is used to discuss the assumptions for the method used. The possibility of extending it to equivalent circuit modeling in general is also treated.

2.1 Overview

This section gives an overview of the direct extraction method and the different sources of uncertainty that enter in the method.

2.1.1 FET small-signal equivalent circuit model

Fig. 2-1 shows a small-signal equivalent circuit commonly used for modeling MES-FETs and HEMTs. It has been shown to be valid up to very high frequencies [14].

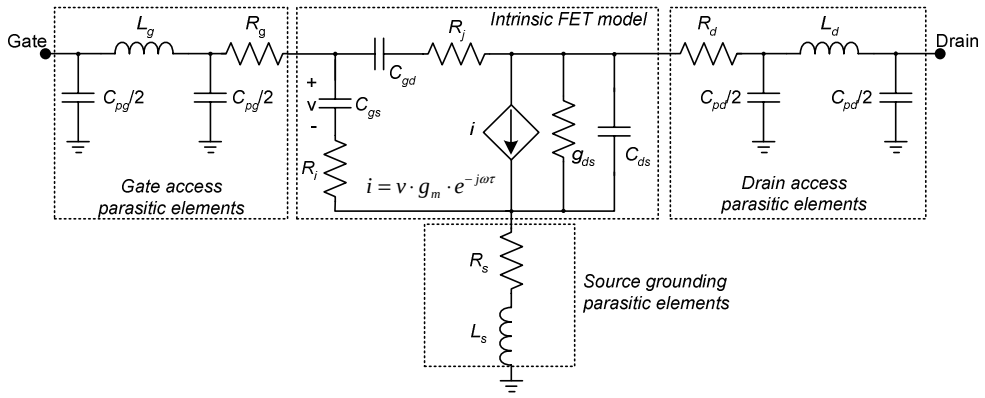

Fig. 2-1. High-frequency FET small-signal model.

The model in Fig. 2-1 is composed of an intrinsic part and parasitic elements representing the connections to access the intrinsic device. The parasitic elements are usually considered bias independent, while the intrinsic FET model parameters are inherently bias dependent and represent the physical phenomena dominating the device operation.

2.1.2 Nomenclature

Before describing methods to accurately determine the model parameters in Fig. 2-1 it is necessary to distinguish between deterministic and statistic model parameter quantities. The terms shown in Fig. 2-2 will be used.

Deterministic		Statistical
Calculated	⟷	Estimated
True parameter value	⟷	Estimated parameter value
Deviation from true parameter value	⟷	Parameter uncertainty
Parameter extraction	⟷	Parameter estimation

Fig. 2-2. Terms used to distinguish between deterministic and statistic quantities in model parameter estimation.

The true model parameter values in Fig. 2-1 are unknown but may be estimated from measurements.

2.1.3 The direct extraction method

For HEMTs and MESFETs, the parameters of the model in Fig. 2-1 are normally estimated using the direct extraction method[1] [12] outlined in Fig. 2-3.

[1] The term *direct extraction* is established and therefore kept as an expression, although *direct estimation* would be more appropriate in this text.

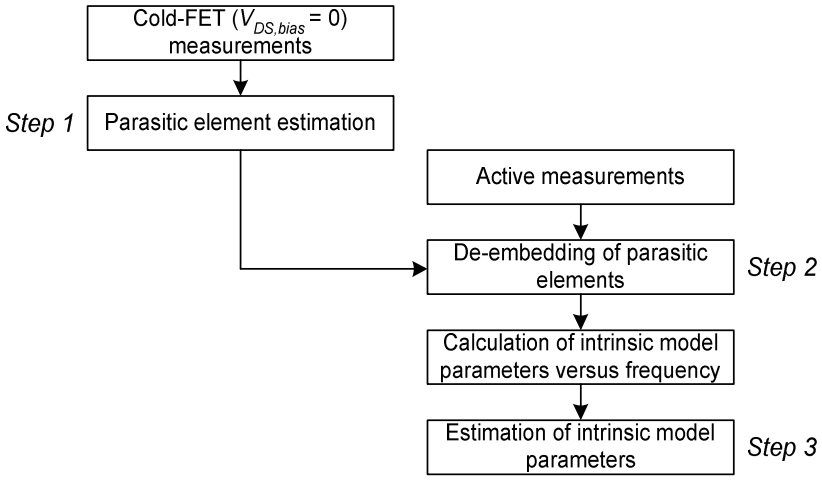

Fig. 2-3. The direct extraction method.

The direct extraction procedure consists of three main steps.

Step 1: Estimation of the parasitic elements

The first step is normally to estimate the parasitic element parameters from measurements at zero drain–source bias voltage ($V_{DS,bias}$) (cold-FET measurements).

Parasitic capacitances are usually estimated from measurement where the gate–source bias voltage ($V_{GS,bias}$) is kept below the turn-on voltage [12, 14]. This simplifies the model in Fig. 2-1, and the parasitic capacitance values can be estimated from the admittance (Y) parameters [12].

The parasitic resistances and inductances are then estimated by forward-biasing the gate–source junction. The resistance and inductance values can then be estimated iteratively [12], whereas for simpler topologies they may be estimated directly from the impedance (Z) parameters [12, 13, 15].

Step 2: De-embedding

After the parasitic elements have been estimated, they are de-embedded from subsequent active measurements.

The most common de-embedding technique is to successively remove the influence of each parasitic element by subtracting its Z- or Y- parameters from the measurement [12]. In this case the de-embedding sequence has to be tailored for a specific parasitic element topology.

A general de-embedding method was presented by Pucel *et al*. [16]. They used a *port-admittance* matrix to represent the parasitic element network between the extrinsic and intrinsic gate- and drain terminals. The same de-embedding equation may thus be used for any parasitic element topology. However, except for trivial cases, the port-admittance matrix can not be derived manually from the parasitic element network.

In [Paper C], we present a general de-embedding method similar to the one in [16], but with a *nodal-admittance* matrix representation of the parasitic element network instead. Contrary to the representation in [16], the nodal-admittance matrix may be derived manually from the parasitic element network using standard circuit theory methods [17]. Hence, a symbolic de-embedding expression can be found, and the influence of individual parasitic elements on the intrinsic behavior can be studied.

Step 3: Estimation of the intrinsic model parameters

The de-embedding algorithms return the intrinsic *Y*-parameters, which are used to calculate the intrinsic model parameters versus frequency [13, 14].

Ideally, the calculated model parameters should present a constant behavior versus frequency, thus making it irrelevant at which measurement frequencies their true values are extracted from.

In practice, stochastic deviations are superimposed on the true values. The calculated model parameters therefore present a stochastic behavior versus frequency, as shown in Fig. 2-4.

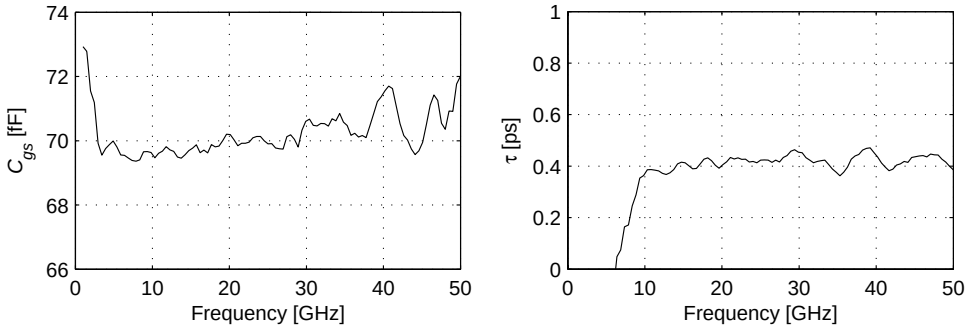

Fig. 2-4. Example of calculated model parameters versus frequency.

The true model parameter values are unknown but normally estimated by simply averaging the calculated model parameters over predetermined frequency ranges. The frequency ranges are found empirically for every parameter depending on the specific device characteristics [13]. This empirical estimation procedure gives no information about the uncertainty in the obtained parameter estimates and may result in erroneous results if wrong frequency ranges are used.

Sources of uncertainty

The stochastic model parameter deviations originate from uncertainties in the estimation method. Two different sources of uncertainty are identified in the direct extraction method, as illustrated in Fig. 2-5.

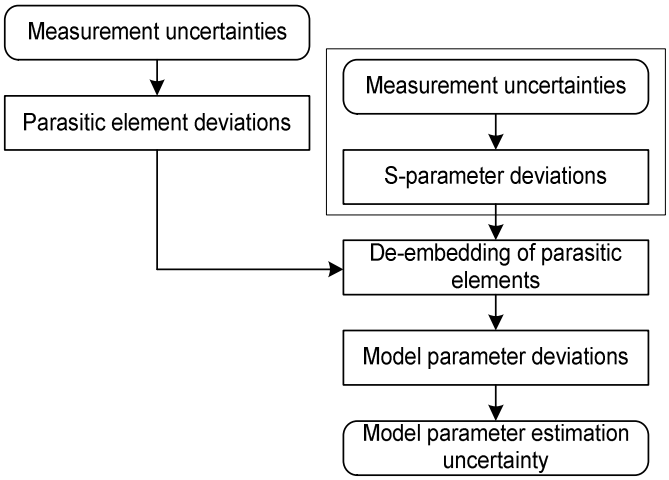

Fig. 2-5. Sources of uncertainty and their resulting deviations in the direct extraction method.

One major source of uncertainty is in the measured *S*-parameters. This is due to limited accuracy of the vector network analyzer (VNA) and the calibrations performed. Walters *et al.* [18] studied the influence of these uncertainties on estimated FET model parameters for different frequencies. No details were given about the uncertainty analysis performed though.

Anholt *et al.* [19] investigated the model parameter sensitivity to parasitic element deviations. They performed a numerical sensitivity analysis, where each of the parasitic elements was manually perturbed 10% and the resulting difference in the estimated model parameters observed. No statistical discussions were presented however.

2.1.4 Statistical model parameter estimation

In [Paper A] and [Paper B], we have presented a comprehensive uncertainty analysis for the direct extraction method. The model parameter uncertainties are analytically derived from measurement and parasitic element uncertainties. These results are used for estimating the model parameters. Similar methods are used in statistical signal processing [20].

This method has, to the best of our knowledge, not been used for model extraction purposes before. It will therefore be described by a simple estimation example in the following section. Details specific for the FET model parameter estimation will be treated separately, in Section 2.3.

2.2 Simple parameter estimation example

A simple *R–C* circuit is used in this section to illustrate the statistical model parameter estimation method. Artificial measurement data, with added normal-distributed noise is used. The true parameter values are then known and the quality of the parameter estimate can be evaluated. Although an ideal case, it illustrates the basic ideas behind the statistical model parameter estimation technique for equivalent circuit models.

2.2.1 Example circuit and measurements

Suppose that noisy *S*-parameter measurements are available over a wide frequency range for a device modeled by the simple *R–C* circuit in Fig. 2-6. This could represent, for example, measurements of S_{22} on the combination of C_{ds} and g_{ds} in the FET model (see Fig. 2-1).

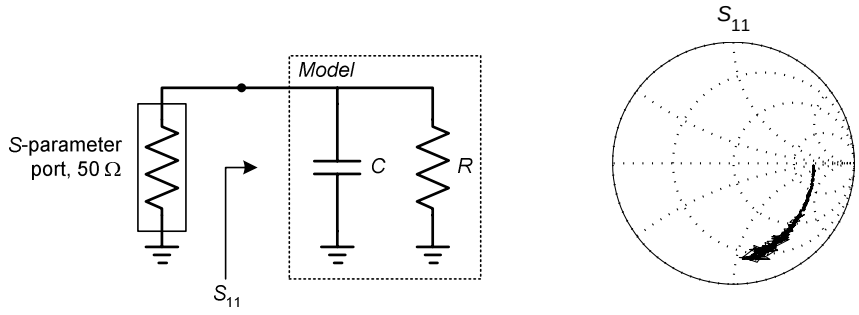

Fig. 2-6. Example R–C circuit model and S_{11} measurement.

Intuitively, the resistance should be estimated from low frequency measurements, since it is short circuited at high frequencies by the capacitance. The capacitance, on the other hand, has high reactance at low frequency and is therefore masked by the resistance in parallel. At high frequency, the measurement uncertainties become larger and the capacitance approaches a short circuit. The capacitance should therefore be estimated at an intermediate frequency range.

Model parameter values versus frequency

The model parameters, R and C, are easily calculated from the real- and imaginary parts of Y_{11} (which is calculated from S_{11}). Fig. 2-7 shows the model parameter values versus frequency.

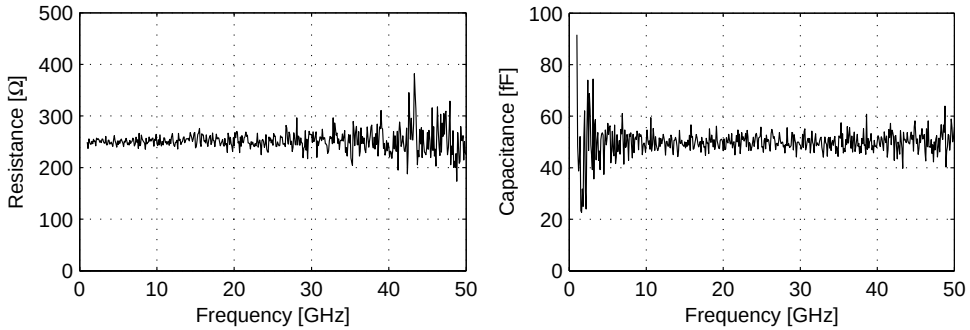

Fig. 2-7. Calculated model parameters versus frequency.

Apparently $R \approx 250\ \Omega$ and $C \approx 50$ fF in this example. Their true values can not be uniquely determined from the measurement but only estimated with some uncertainty. These uncertainties should be quantified by e.g. confidence intervals, and presented together with the estimated values for R and C. For this purpose an uncertainty analysis is needed as described in the following section.

2.2.2 Uncertainty analysis

To allow for the following analysis we need to consider the true model parameter values as being known. The variations observed in Fig. 2-7 are stochastic deviations from the true R and C values.

The model parameter deviations are transformed from deviations in the measured S-parameters. This transformation is nonlinear but, since the deviations are usually small, it may be linearized. A first-order sensitivity analysis may therefore be used to relate the S_{11} deviations to the deviations in R and C.

Sensitivity analysis

Sensitivity analysis is often included in electrical computer aided engineering (CAE) programs, where it is used to quantify how sensitive an output signal is to deviations in internal circuit parameters [21]. However, generally, these sensitivity analyses can not be used for our intended purpose. We are interested in the opposite situation, i.e. how sensitive the internal circuit parameters (R and C) are to deviations in an output signal (S_{11}).

The relative sensitivity[2] (K), which will be used here, tells the percentage change in e.g. R for a 1% change in $|S_{11}|$. Mathematically this is expressed by

$$\frac{\Delta R}{R} \cong \frac{\partial R/R}{\partial |S_{11}|/|S_{11}|} \frac{\Delta |S_{11}|}{|S_{11}|} = \mathrm{K}^{R}_{|S_{11}|} \frac{\Delta |S_{11}|}{|S_{11}|}, \tag{2-1}$$

which also gives the definition of the sensitivity in R to S_{11} magnitude deviations, $\mathrm{K}^{R}_{|S_{11}|}$. A similar expression is used for phase sensitivities,

$$\frac{\Delta R}{R} \cong \frac{\partial R/R}{\partial \angle S_{11}} \Delta \angle S_{11} = \mathrm{K}^{R}_{\angle S_{11}} \Delta \angle S_{11}. \tag{2-2}$$

Absolute phase deviations are used since the phase already is a relative measure of the arc-length to the radius.

Fig. 2-8 shows how the sensitivities are used to calculate the model parameter deviations from the *S*-parameter deviations. The *Y*-parameters are used as an intermediate step to ease the sensitivity calculations as illustrated in the figure.

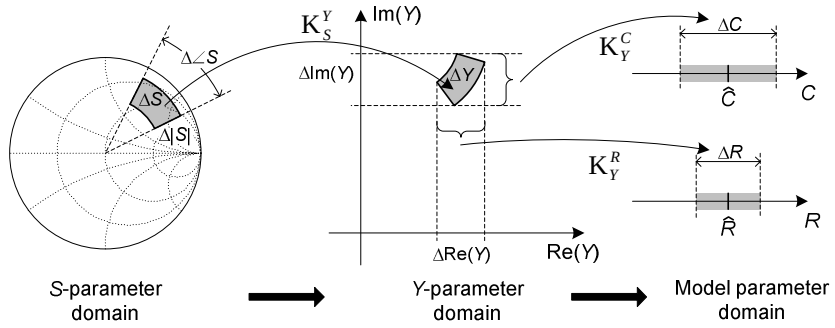

Fig. 2-8. Illustration of how the sensitivities (K) are used to calculate the model parameter deviations from deviations in the S-parameter measurement. The Y-parameter domain is used intermediately to ease the sensitivity calculations.

The resulting model parameter sensitivities to deviations in the S_{11} magnitude and phase are shown versus frequency in Fig. 2-9.

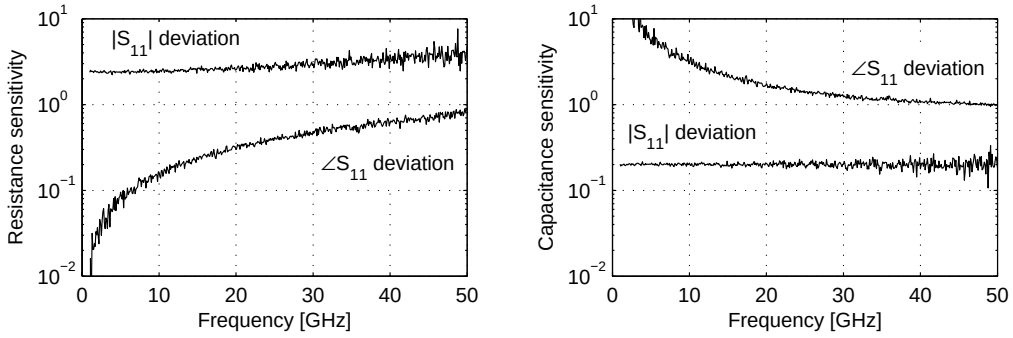

Fig. 2-9. Frequency dependence of the relative model parameter sensitivities to deviations in the S-parameter magnitude and phase.

[2] Hereafter only relative sensitivities will be treated. The word *relative* will therefore be omitted.

Fig. 2-9 shows that R is most sensitive to $|S_{11}|$ deviations, whereas C is more sensitive to deviations in $\angle S_{11}$, as expected. In order for a parameter to be well defined, its sensitivities should be small since the sensitivity to measurement noise will then also be low.

In Fig. 2-9, the resistance has smaller sensitivity at low frequency, although it is quite low over the entire frequency range. The capacitance, on the other hand, has a sensitivity that decreases at higher frequencies, indicating that it is more well-defined there. However, to know where it is most well-defined, the measurement uncertainties must also be considered.

Uncertainty representation

The *S*-parameter deviations arise from measurement uncertainties that are random and thus described by probability distributions. The exact distributions are usually unknown. In practice, however, they are often assumed to be normal distributed. This may be partially justified by the central limit theorem, since each of them is composed of a large number of small and reasonably independent uncertainty contributions [22].

The *S*-parameter magnitude and phase deviations are normal-distributed with zero mean and known variances (σ^2) in this example. It is also assumed that these deviations are independent. The model parameter variances may then be calculated using the sensitivities in (2-1) and (2-2) together with well-known variance formulas [22]:

$$\sigma_R^2 = \left(\mathrm{K}_{|S_{11}|}^{R}\right)^2 \sigma_{|S_{11}|}^2 + \left(\mathrm{K}_{\angle S_{11}}^{R}\right)^2 \sigma_{\angle S_{11}}^2 \tag{2-3}$$

$$\sigma_C^2 = \left(\mathrm{K}_{|S_{11}|}^{C}\right)^2 \sigma_{|S_{11}|}^2 + \left(\mathrm{K}_{\angle S_{11}}^{C}\right)^2 \sigma_{\angle S_{11}}^2 . \tag{2-4}$$

Fig. 2-10 shows the resulting model parameter uncertainties versus frequency. The uncertainties are indicated by $\pm 2\sigma$ error bars, corresponding to 95% confidence intervals for the normal distribution.

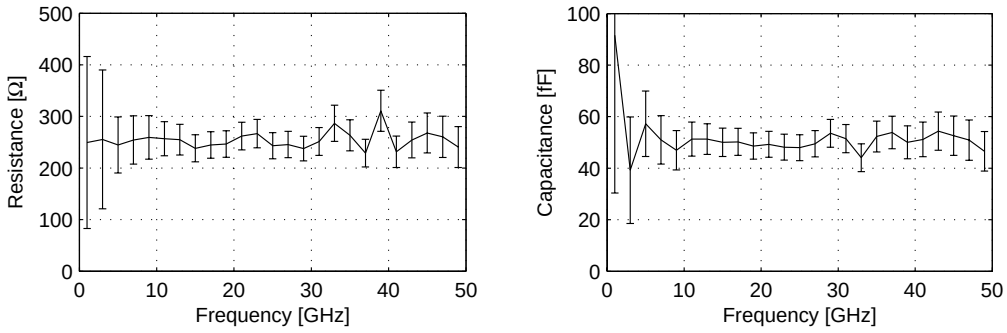

Fig. 2-10. Calculated model parameters and their estimated uncertainties versus frequency. The error bars display a 2σ (95%) confidence interval.

2.2.3 Parameter estimation

In traditional estimation methods, the calculated model parameter values are simply averaged over a predetermined frequency range. However, with knowledge about the parameter uncertainties, a weighted average may be performed to improve the

estimate. The estimation uncertainty is minimized by assigning less weight to more uncertain extractions and vice versa. The appendix of [Paper A] describes how this is done.

As previously mentioned, the uncertainty analysis needs the true model parameter values. Initially, we use the frequency dependent values in Fig. 2-7 for the uncertainty analysis. As new estimates are made, the uncertainty analysis is refined. The model parameter estimates are not very sensitive to the uncertainty analysis results and three iterations are normally sufficient.

The resulting parameter estimates for this example become:

$$\begin{cases} \hat{R} = 249.72 \pm 0.91 \ [\Omega] \\ \hat{C} = 49.82 \pm 0.28 \ [\text{fF}] \end{cases}, \tag{2-5}$$

where a 95% confidence interval is also given. Since the *S*-parameters were normal-distributed, and only linear operations have been used, the estimated model parameters will also be normal-distributed with mean- and variances given from (2-5) above.

The model parameter estimates correspond well to the true values used for generating the artificial measurement data: R = 250 Ω and C = 50 fF.

In this example, the $\hat{R}$ and $\hat{C}$ distributions become uncorrelated. This is due to the fact that they are extracted independently from the real and imaginary parts of Y_{11}, respectively. This is generally not the case. Correlations between the estimated parameters can be determined by using the formal statistical method presented in [Paper B].

2.2.4 Uncertainty in the modeled response

It is often desired to know the uncertainty also in the modeled *S*-parameters. This may be the case when a FET manufacturer supplies a device model. As a user of this model, we may want to know the design margins for a certain gain. Such information is usually not available.

It is possible to use the sensitivity analysis again, but now in the reverse direction, to get this information. This is illustrated in Fig. 2-11.

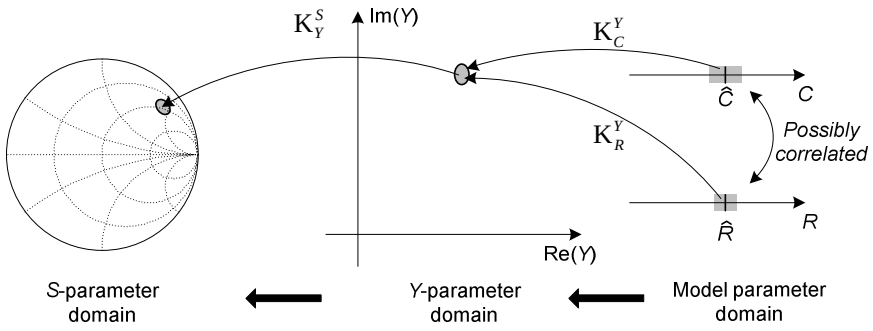

Fig. 2-11. Illustration of how the sensitivities (K) are used to derive the modeled S-parameter uncertainties from uncertainties in the estimated model parameters.

Fig. 2-12 shows confidence intervals for the magnitude and phase of the original S_{11} measurement and the estimated model.

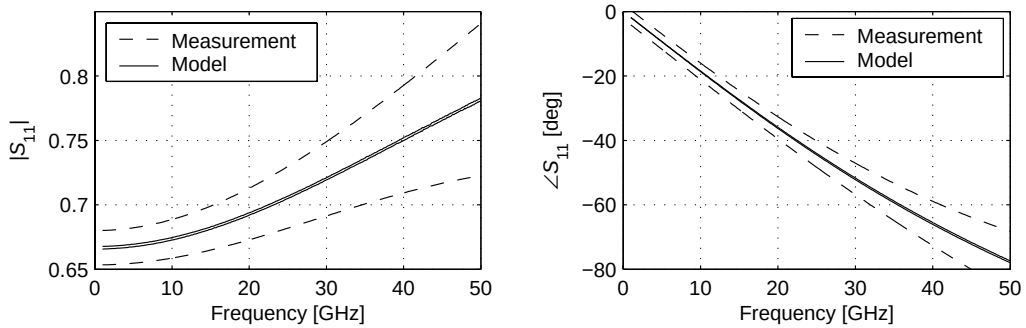

Fig. 2-12. Estimated 95% confidence interval for measured and modeled S_{11}. Note that the model confidence interval is very narrow and appears as a single line.

It might seem counterintuitive that the model can represent the device better than the measurement it was extracted from, as seen in Fig. 2-12. This originates from the assumption that the chosen model topology is correct. A very accurate estimation of the two model parameters *R* and *C* can then be made by collecting information from S_{11} measurements over the entire frequency range. Everything in the measurements that does not match the set of possible *S*-parameter frequency responses is treated as noise.

However, in practice, it is a matter of philosophy whether to rely on the model topology or the measurement.

2.3 FET model parameter estimation

The same method used for estimating the *R*–*C* model parameters in the previous section has been applied to estimate the FET model parameters in [Paper A] and [Paper B]. This section reviews the FET model parameter estimation method and presents applications of the results obtained.

2.3.1 Uncertainty contributions

A first-order sensitivity analysis, similar to the one used in the *R*–*C* example, has been used for the FET model uncertainty analysis. Fig. 2-13 illustrates how the sensitivities are used for calculating the model parameter uncertainties in the direct extraction process.

The model parameter uncertainties are related to the *S*-parameter uncertainties in [Paper A]. These results are generalized in [Paper B] where also the uncertainty contribution from parasitic elements is investigated. The *S*-parameter- and parasitic element uncertainties in Fig. 2-13 need therefore to be quantified before the model parameter uncertainties can be estimated.

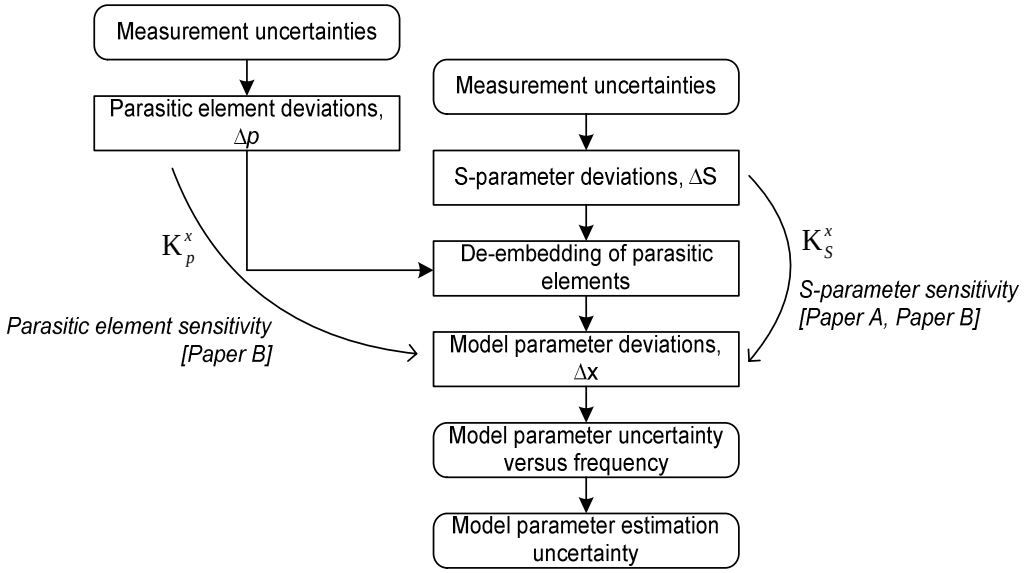

Fig. 2-13. Model parameter sensitivities to S-parameter and parasitic element deviations. Intermediate steps used in the sensitivity calculations are omitted.

S-parameter uncertainty

The *S*-parameter uncertainties have several contributions, e.g. knowledge about the calibration standards, the type of calibration performed, and contact repeatability. The *S*-parameter measurement uncertainties are generally difficult to estimate.

Williams *et al*. [23] presented a method to estimate the measurement uncertainties in on-wafer measurements by comparison with a reference thru-reflect-line (TRL) calibration.

Another common method to evaluate the measurement uncertainties is by measurements on a high impedance transmission line standard whose response may be predicted accurately [24, 25]. The measurement error may thus be calculated as the difference between the measurements and the theoretical predictions. Using this method together with careful on-wafer probed TRL and line-reflect-match (LRM) calibrations we have found the uncertainties obtained to be close to the ones specified for the VNA[3].

In [Paper A], we have developed *S*-parameter uncertainty models from the Agilent 8510C VNA *worst-case* uncertainty specifications shown in Fig. 2-14 [26].

[3] The uncertainty specifications are given for coaxial measurements under well-defined conditions given in [26] "8510C Network Analyzer Data Sheet," Agilent Technologies 1999.

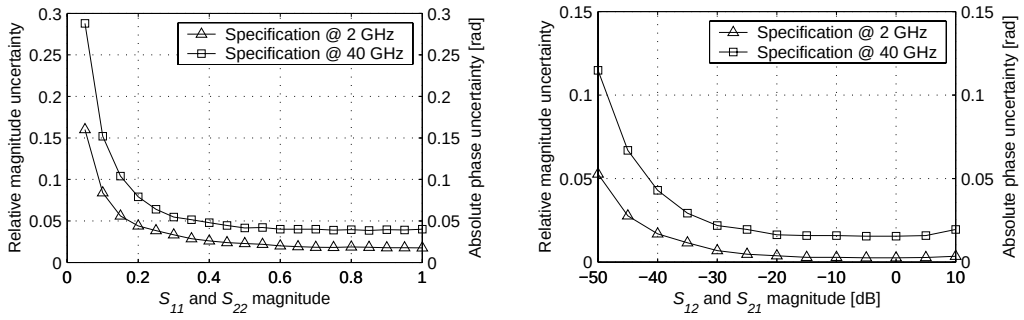

Fig. 2-14. Example of VNA worst-case measurement uncertainty specifications.

The VNA uncertainties depend on the measured *S*-parameter magnitudes and frequency as seen in Fig. 2-14. We have further assumed that the uncertainties at different measurement frequencies are uncorrelated. More comprehensive VNA uncertainty models can be found at [27].

Any of these uncertainty models may be implemented with the estimation method presented in [Paper B].

Parasitic element uncertainty

The parasitic elements are estimated using separate cold-FET measurements prior to the active measurements. Once estimated, the parasitic element values are fixed and used for de-embedding the active measurements at all frequencies. Uncertainties in the parasitic element values will therefore influence the model parameters at *all* frequencies.

The influence of parasitic element uncertainties has been studied in [Paper B]. There, empirically uncertainties were assumed for them. However, their uncertainties originate from cold-FET measurement uncertainties and the method used to determine them.

Probe position uncertainty

The probe positions are uncertain in relation to the designated nominal reference plane during on-wafer measurements, as illustrated in Fig. 2-15.

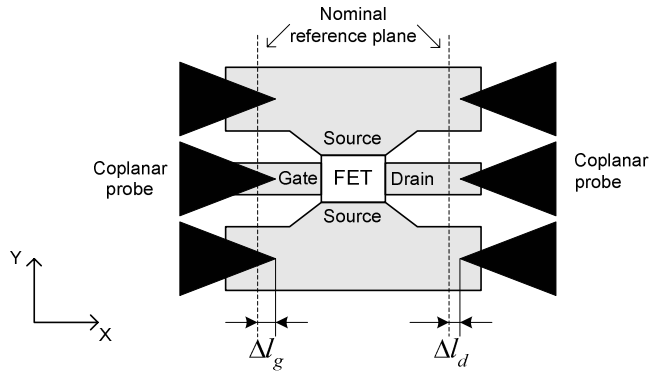

Fig. 2-15. On-wafer probe position uncertainties.

Walters et al. [18] have studied the influence of probe position uncertainties for the case of automated probe positioning across a wafer. The probe separation was assumed accurate, but it was estimated that the probes could be displaced up to 20 µm

in the X-direction (see Fig. 2-15). Displacement in the Y-direction was neglected. In our opinion it will have minor impact.

The gate- and drain parasitic element networks in Fig. 2-1 may be considered as lumped element representations of transmission lines [14]. In [Paper B] we propose that the probe displacement may be modeled as a corresponding deviation in the length of these transmission lines, which results in parasitic capacitance and inductance uncertainties. These uncertainty contributions are therefore treated in the same way as parasitic element uncertainties.

2.3.2 Model parameter uncertainties and estimation

In [Papers A and B], the *S*-parameter uncertainty contribution is used to estimate the model parameters. The uncertainty in the estimation is then dominated by the parasitic element uncertainty contribution as demonstrated in [Paper B].

***S*-parameter uncertainty contribution versus frequency**

Fig. 2-16 shows the *S*-parameter uncertainty contribution obtained for two of the model parameters in [Paper B]. The measurements are made on an indium-phosphide (InP)-HEMT device [28], biased for amplifier operation.

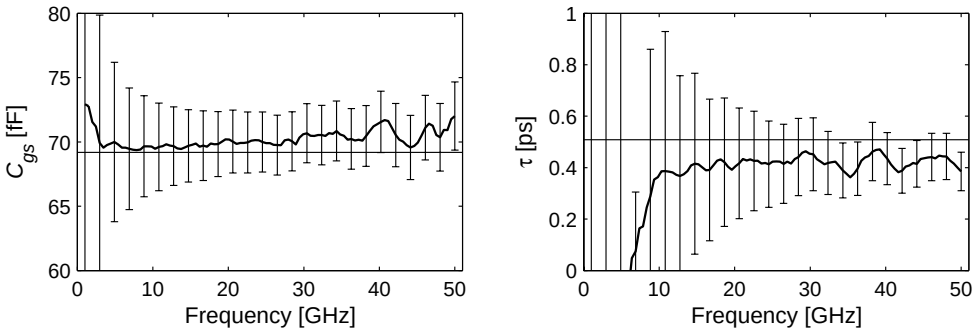

Fig. 2-16. Calculated model parameters versus frequency with their S-parameter uncertainty contributions illustrated by 95% confidence interval error bars. The horizontal line corresponds to the Best Linear Unbiased Estimator (BLUE) parameter estimation.

Optimal weighted average

As mentioned in the previous section, an optimal weighted average method may be used to estimate the true model parameter values. At each frequency, the calculated model parameter value is assigned a weighting factor related to its uncertainty. The uncertainty in the averaged model parameter estimate is thereby minimized [Paper A].

This estimation is performed on each model parameter individually, without considering correlation between them. It is further required that the model parameter uncertainties for different frequencies are uncorrelated, which may not be the case if a detailed *S*-parameter uncertainty model is used.

The Best Linear Unbiased Estimator

The general problem of estimating model parameters from uncertain measurements is commonly treated in statistical signal processing [20].

For the FET model estimation problem, it is possible to use the Best Linear Unbiased Estimator (BLUE) [20], [Paper B]. The BLUE may be considered as a generalization of the optimal weighted average method, but it is also capable of handling any kind of present covariances. This facilitates the use of a very realistic uncertainty model in the estimation.

In Fig. 2-16, the BLUE estimate of the model parameters are shown as horizontal lines. The estimates are slightly offset compared to the measured values. Most likely this is due to covariance between the measured parameters. The BLUE estimates presented are optimal in a global sense where correlations between different model parameters are considered.

In addition to optimal estimation, the BLUE also gives the covariance matrix for the estimated parameters. Its diagonal elements are the estimation variances, and thus quantify the estimation uncertainty. However, for a consistent statistical representation of the estimation uncertainty, the complete covariance matrix is needed. The estimation uncertainty may then be accounted for and set in relation to other kinds of statistical model parameter variations, such as FET processing variations.

Only the *S*-parameter uncertainty contributions were used with the BLUE in [Paper B]. The model parameter estimation uncertainties due to *S*-parameter uncertainties become very small compared to the uncertainty contributions from the parasitic elements.

Influence of uncertainties in parasitic elements and probe positioning

Fig. 2-17 shows the influence of parasitic element and probe positioning uncertainties versus frequency for two of the parameters estimated in [Paper B].

The frequency range with the lowest *S*-parameter uncertainty contribution dominates the model parameter estimation. The parasitic element uncertainty contribution will therefore be determined from the frequency range with the lowest *S*-parameter uncertainty contribution. This is also true for the probe positioning uncertainties.

In Fig. 2-17, C_{gs} will approximately be determined within the frequency range 20 to 50 GHz. The probe positioning uncertainty contribution will therefore be approximately 6–8% and dominate the total parameter estimation uncertainty. For τ, the total estimation uncertainty will be ≈10%.

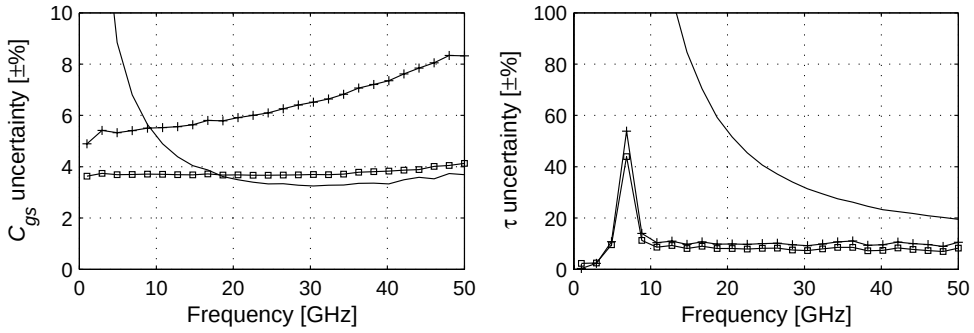

Fig. 2-17. The individual uncertainty contributions from the parasitic elements (□),the probe position (+), and the S-parameters (—).

2.3.3 Uncertainty in the modeled response

Similar to the *R*–*C* example, the sensitivity analysis in [Paper A] has also been used in the reverse direction to calculate the uncertainty in the modeled *S*-parameter response. Fig. 2-18 shows the obtained results.

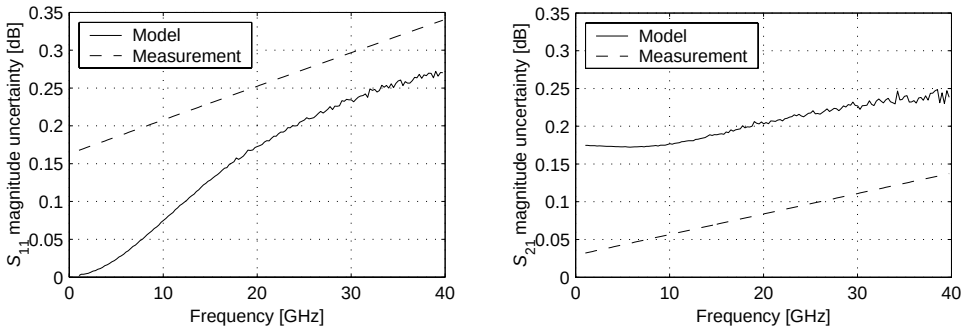

Fig. 2-18. S-parameter uncertainty for the estimated model (Model) and the measurement it was estimated from (Measurement).

It is interesting to note that the uncertainty in the modeled S_{11} response approaches zero at low frequency. This is due to the chosen model topology, see Fig. 2-1. It forces the input impedance to become infinite ($S_{11} \equiv 1$) at low frequency, independent of any model parameter or the measured S_{11}. $|S_{21}|$ has no such restrictions and may take any value. The modeled $|S_{21}|$ uncertainty is therefore non-zero and, in this case, higher than the measurement it was estimated from.

The calculations in Fig. 2-18 are based on the sensitivity analysis in [Paper A], where the parasitic element uncertainties were not considered. The model parameters were further estimated from non-overlapping frequency ranges. The model parameter uncertainties are then independent, which was required for the analysis.

A further step will be to perform the model response uncertainty calculations in [Paper A] using the sensitivity and uncertainty analyses in [Paper B]. This would allow the parasitic element uncertainties to be considered and thus give a better indication of the expected model response uncertainty.

2.4 Discussion and applications

In our work we have performed a systematic analysis of the influence of uncertainties present during the FET model parameter estimation process. This allowed us to develop a statistical FET model parameter estimation method in [Paper A] and [Paper B]. Similar methods are used in statistical signal processing applications but have, to our knowledge, never been applied to equivalent circuit modeling before.

2.4.1 Assumptions

Our estimation method has been based on the following assumptions:

All measurement uncertainties are normal distributed with known variances

It is usually a reasonable assumption that the measurement uncertainties are normal distributed. Even if this is not exactly the case, it does not have a severe impact since several independent contributions are added in the estimation method. Their

combined effect approaches a normal distribution according to the central limit theorem.

However, it is usually not possible to accurately know their variances, and empirical uncertainty models need to be used [29]. The consequence of such errors is typically that the uncertainties in the model parameters are under- or overestimated, however, without much influence on the parameter estimate itself.

A first-order sensitivity analysis can be used

The *S*-parameter measurement and parasitic element uncertainties are usually small. Even so, we have experienced that a first-order sensitivity analysis may be insufficient in some cases.

Neglecting higher order sensitivities is expected to have minor effect on the model parameter estimates since the uncertainty analysis only concerns the weighting of the calculated model parameters versus frequency. The accuracy of the derived estimation uncertainty could be affected though. Nevertheless the obtained estimation uncertainty is probably less than in traditional methods where the uncertainties are not considered at all.

The model topology is correct

The entire concept of estimating model parameters becomes doubtful if the measurements are made on a device which can not be represented by the chosen topology. This is a common problem in all estimation methods.

True model parameter values exist

The true model parameters have been considered as deterministic and defined from physical properties of the device.

An alternative approach is to consider the true model parameter values as being stochastic. This is the case when *Bayesian estimation* is used [20]. In that case, no unique values exist for the true model parameters but rather probability density functions (PDF). These PDFs represent *a priori* knowledge of the parameters. The model parameter estimate is formed by combining the prior knowledge with the results obtained from measurements. The prior knowledge could in our case be used to reject nonphysical negative parameter values.

2.4.2 Applications

FET process monitoring

As part of monitoring their process variations [30] FET device manufacturers and monolithic microwave integrated circuit (MMIC) foundries usually perform model extractions for every wafer and process batch. The resulting model parameters are stored in a database for statistical evaluation [31]. Moreover, MMIC foundries usually implement model parameter statistics in their FET models. This allows circuit designers to account for the process variations.

However, since no methods, except for the ones in [Paper A] and [Paper B], are available to evaluate the uncertainty in the extracted model parameters, it might happen that parameter variations interpreted as originating from process variations are in fact due to measurement uncertainties.

Statistical simulations

Monte-Carlo simulations are commonly used to study the influence of FET model statistics on circuit performance [2]. These simulations may be combined with an optimizer to perform *yield optimization*, in which the circuit parameters are tuned to maximize the fraction of manufactured circuits satisfying the circuit specifications [32].

The modeled response uncertainty due to model estimation uncertainties was predicted from the sensitivity analysis in Section 2.3.3. If the model parameter uncertainties due to manufacturing process variations are reasonably small and normal-distributed, the same method could also be used for predicting their influence on circuit performances. The need for time-consuming Monte Carlo simulations could thus be eliminated.

Automatic multi bias model parameter estimation

The estimation method presented in [Paper A] and [Paper B] requires very little extra information compared with normally used FET model extraction methods. Considering also that the method performs optimal estimations independent of the device characteristics or the bias point, it should be attractive for implementation in automatic multi bias model extraction software. As an added feature, the method automatically reports the uncertainty in the performed estimation.

It should be noted that the same method used for estimating the intrinsic model parameters could be implemented also for the cold-FET extraction of the parasitic elements. That would provide good estimates for the parasitic elements and their uncertainties, which is required for the intrinsic model parameter estimation above.

Other applications

In our work we have applied the model parameter estimation method to FETs. It may as well be applied to equivalent circuit models for other devices, such as bipolar transistors, diodes, or any other electrical device or circuit having an associated model, as long as the assumptions above are fulfilled.

Chapter 3. Analysis of intermodulation distortion in FET power amplifiers

Modern communications systems use complex amplitude- and phase modulation schemes to maximize the transmission capacity [3]. Very low levels of nonlinear intermodulation distortion (IMD) are then required in the transceiver components to prevent errors in the transmitted data [33, 34]. The IMD also appears as sidebands to the desired transmitted signal that can mask adjacent weaker signals.

The dominant origin of IMD in the transmitter is usually power amplifier (PA) nonlinearities. The IMD specifications must therefore be considered together with output power and efficiency requirements when designing PAs for such applications. As a compromise, PAs are typically operated at high input power levels and biased close to the turn-on voltage for class AB operation [35].

The input signal cannot be considered as a small perturbation from a fixed bias point under these conditions. Still, PA IMD is often analyzed using weak-signal methods where low-order Taylor-series representations of the nonlinearities are used.

Accurate PA IMD prediction requires that a true large-signal analysis is performed. However, contrary to output power and efficiency, no analysis methods exist that allow the origins of PA IMD behavior to be understood under realistic large-signal conditions. Empirical, numerical, or even weak-signal methods are therefore used to determine the compromise between output power, efficiency, and IMD in PA design. The results obtained cannot reveal the mechanisms generating IMD. Hence, suboptimal performance may result.

The first section of this chapter gives an overview of nonlinear PA operation. Commonly used IMD figures-of-merit (FOMs) and methods to characterize IMD in PAs are then described. An overview of IMD analysis methods is also given.

Section 3.2 reviews commonly used weak-signal IMD analysis methods. These methods serve as a background for understanding large-signal IMD behavior.

Large-signal analysis methods are treated in Section 3.3. In particular, our work on analytical large-signal IMD analysis methods is described. These methods allow the mechanisms responsible for measured large-signal IMD behavior to be identified and understood. Numerical simulation methods otherwise used to predict large-signal IMD are also reviewed.

Section 3.4 discusses large-signal models for IMD prediction. These are used in combination with numerical IMD simulation methods for detailed IMD prediction. Different methods to test the suitability of large-signal models for this purpose are described. We have applied such methods to evaluate commercially used LDMOSFET and MOSFET models.

Conclusions are drawn in the final section.

3.1 Overview

This section reviews basic PA concepts and commonly used IMD characterization methods. An overview of the IMD analysis methods treated is given at the end.

3.1.1 Basic power amplifier operation

Fig. 3-1 shows a general representation of a FET PA circuit. MOSFET devices are treated as three-terminal devices by assuming that the body and source terminals are connected.

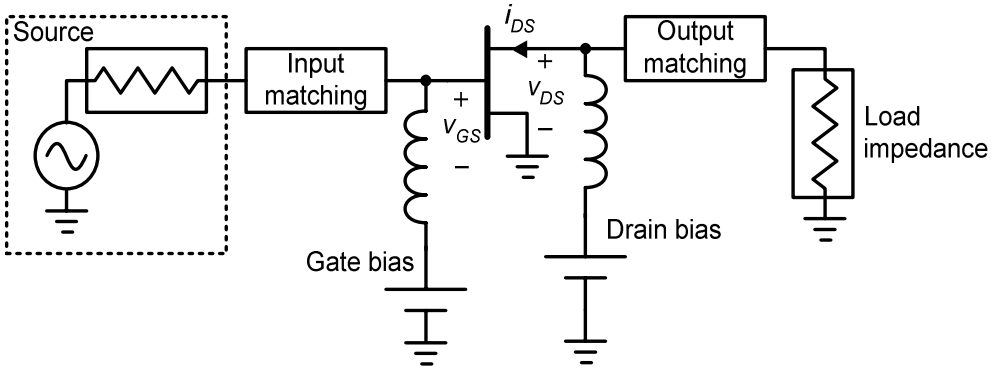

Fig. 3-1. General power amplifier circuit representation.

The dynamic drain–source voltage (v_{DS}) and dynamic drain–source current (i_{DS}) are related by a trajectory for a given load-impedance and $V_{DS,bias}$, with the dynamic gate–source voltage (v_{GS}) being the independent variable. This trajectory is called the *load-line* and is plotted with the dc I_{DS}/V_{DS} characteristics in Fig. 3-2(a).

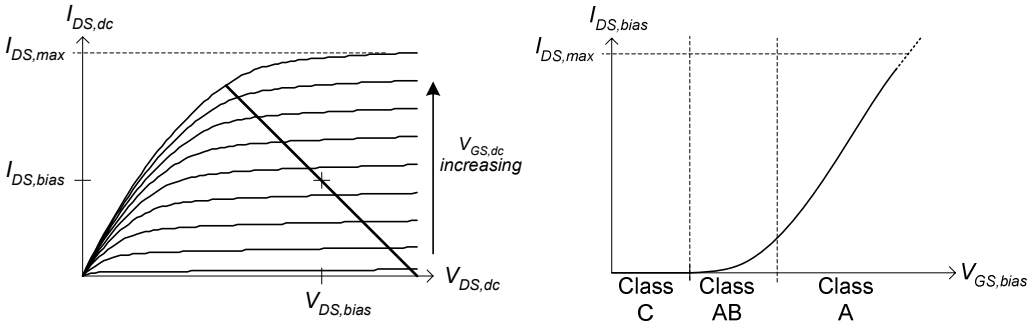

(a) (b)

Fig. 3-2. (a) Typical FET dc I_{DS}/V_{DS}-characteristics (thin lines) and load-line (thick line) for power amplifier operation; (b) I_{DS}/V_{GS} characteristic with the drain bias assumed to be in the saturated region. The class of operation is defined from the gate–source bias voltage ($V_{GS,bias}$).

The RF output power is maximized when the load-line has its extreme points reaching the maximum voltage and current limits, as shown in Fig. 3-2(a). This is achieved by adjusting the load-impedance and $V_{DS,bias}$ [36].

The device in Fig. 3-2(a) is biased in the middle of the saturated region. This corresponds to class A operation. The classic classes of operation are defined from the gate–source bias voltage ($V_{GS,bias}$) as illustrated in Fig. 3-2(b).

Practical PAs are usually biased towards class AB or class C to improve efficiency [35]. However, more input power is then required to maintain the same output power. This limits the overall efficiency improvement.

Detailed methods to predict output power and efficiency are described in [36].

3.1.2 PA IMD behavior and characterization methods

Before IMD prediction methods are treated, some commonly used methods to characterize IMD in PAs are reviewed. Measurements of a CMOS PA are used to exemplify typical behavior [Paper E].

Two-tone measurements

PA IMD is traditionally tested by two-tone measurements. Two sinusoidal signals with narrow frequency separation are simultaneously applied to the PA input. Due to the PA nonlinearities, IMD sidebands will emerge in the output signal, as illustrated in Fig. 3-3.

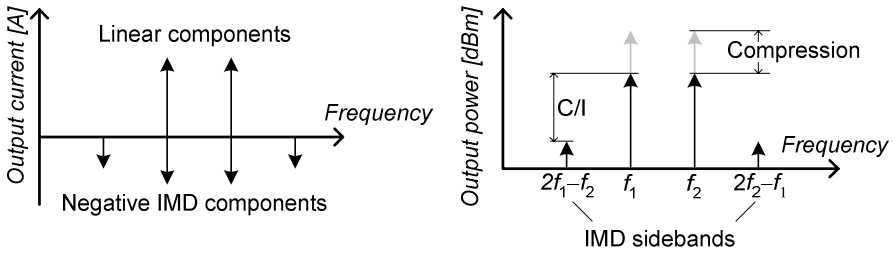

Fig. 3-3. (a) Output current components generated from a third-order nonlinearity; (b) Measured output power spectrum.

In practice, more IMD sidebands will appear adjacent the ones shown in Fig. 3-3. However, the IMD sidebands in Fig. 3-3 are usually dominant. IMD is therefore, hereafter, referring to these sidebands if not otherwise mentioned.

Fig. 3-3(a) shows that IMD is generated not only as sidebands, but also on top of the desired frequency components. The sign of the IMD components determines if the output power is expanded or compressed compared to the linear, undistorted, response. This also indicates the strong relationship present between one-tone gain characteristics and IMD behavior [37].

Fig. 3-4 shows an illustration of two-tone measurement results commonly expected. The extrapolated input/output third-order intercept point (IIP3/OIP3) FOMs are also defined in the figure.

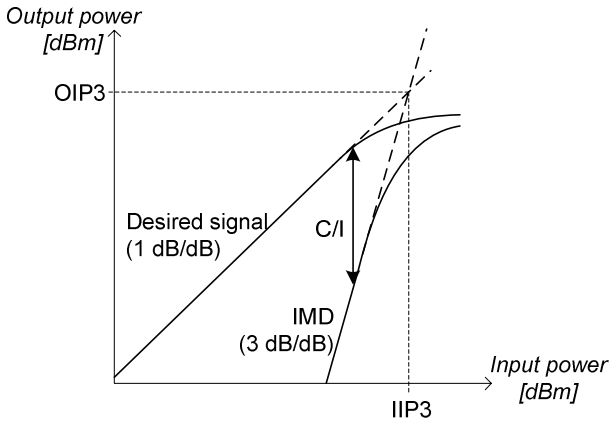

Fig. 3-4. Idealized two-tone measurement results. The third-order input/output intercept point (IIP3/OIP3) figures of merit and the carrier-to-intermodulation (C/I) defined in the figure.

The behavior in Fig. 3-4 appears if a *weakly* nonlinear PA is measured, in which the device nonlinearities may be accurately represented by a third-order Taylor-series expansion (cf. Section 3.2). For most practical PAs, this assumption fails as already discussed. Particularly for LDMOS and CMOS PAs this is true as shown in [Paper D] and [Paper E], respectively.

Two-tone measurements obtained in class C and class AB for a practical CMOS PA are shown in Fig. 3-5 [Paper E].

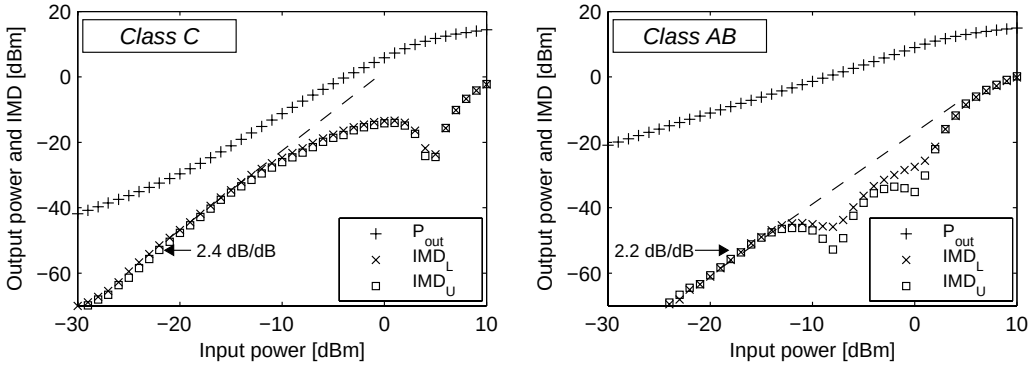

Fig. 3-5. Measured two-tone output power and IMD power levels versus input power for class C and class AB operation. IMD_L and IMD_U correspond to measurements of the lower- and upper IMD sidebands, respectively.

First, it is observed that the IMD slope is far from being three even at very low input power levels in Fig. 3-5. A slope of three is predicted for a weak nonlinearity. IIP3 and OIP3 therefore become misleading for the PA IMD performance. Yet these FOMs are often reported for PAs.

Second, both measurements in Fig. 3-5 present irregular IMD versus input power behavior. For class C, one IMD minimum (sweet-spot) is observed close to the compression point, whereas two sweet-spots appear at intermediate power levels in class AB. Especially for class AB, these sweet-spots are very beneficial since their combined effect improve the IMD performance over a wide input power range. The

mechanisms behind both these characteristics may be explained using the analysis methods in Section 3.3.

Third, the class AB measurements present IMD asymmetries between the upper and lower sidebands. Carvalho and Pedro [38] explained that this originates from either reactive base-band impedance at $f_1 - f_2$ or reactive device nonlinearities. This is also treated in [35] and has important implications on the IMD performance when wideband signals or linearization techniques are applied [39].

Wideband IMD measurements

Two-tone measurements are nowadays often replaced by measurements with a wideband input signal. The wideband signal has statistical properties more similar to the ones used in real applications.

Fig. 3-6 shows the distorted output signal spectrum for a wideband code division multiple access (W-CDMA) input signal.

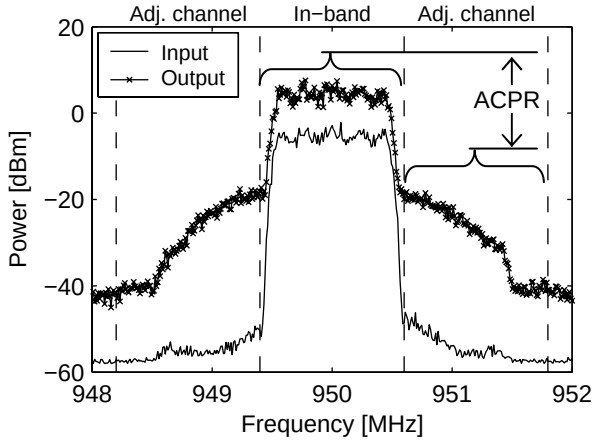

Fig. 3-6. Example of PA output signal spectrum for a wideband input signal. Adjacent channel power ratio (ACPR) relates in-band total power to the IMD power in an adjacent channel.

Fig. 3-6 shows that the PA nonlinearities create a broadening of the input spectrum (spectral regrowth) rather than discrete sidebands as in the case of a two-tone input signal.

The wideband input signal may be considered as being composed of an infinite number of sinusoidal components. To a first approximation, each combination of two sinusoidal components may be interpreted in the same way as the two-tone measurements above. The resulting IMD level is determined from the device nonlinearity and the number of frequency combinations resulting in a particular frequency. The probability that the two frequencies considered are widely separated is small. The IMD level will therefore decrease with the distance from the input signal bandwidth, thus creating the typical spectral regrowth pattern shown in Fig. 3-6.

For weakly nonlinear circuits, it is possible to relate the wideband and two-tone measurements. Pedro and Carvalho [40] presented a detailed treatment of this subject.

IMD is commonly specified as the adjacent channel power ratio (ACPR) for wideband input signals. ACPR is defined as the total integrated power in either of the adjacent channels related to the total power in the desired channel, and corresponds to C/I in the two-tone case.

Discussion

Many of the fundamental IMD phenomena observed in two-tone measurements also appear for wideband input signals despite their completely different statistical properties. This is the case for e.g. IMD sweet-spots and asymmetries. However, the input power is stochastic for wideband signals, which tends to smear out the IMD characteristics compared to the two-tone measurements. Improvements in two-tone IMD behavior will nevertheless result in corresponding improvements when a realistic wideband input signal is applied [Paper E].

The IMD analysis methods presented in the following sections assume a two-tone input signal if not otherwise mentioned.

3.1.3 Intermodulation distortion analysis methods

The IMD behavior observed in PAs results from an interaction between the device nonlinearities and the embedding circuit. Generally, no closed-form solutions can be found for the resulting IMD and iterative numerical analysis methods, such as harmonic-balance, are used.

Analytical PA IMD analysis may still be performed under certain simplifying assumptions. The following two sections focus on such analysis methods. They can be used to understand how IMD is generated, and thus how it may be improved in PAs.

The methods treated are categorized according to the input power regimes they are suited for as weak- and large-signal analysis methods (*see* Fig. 3-7).

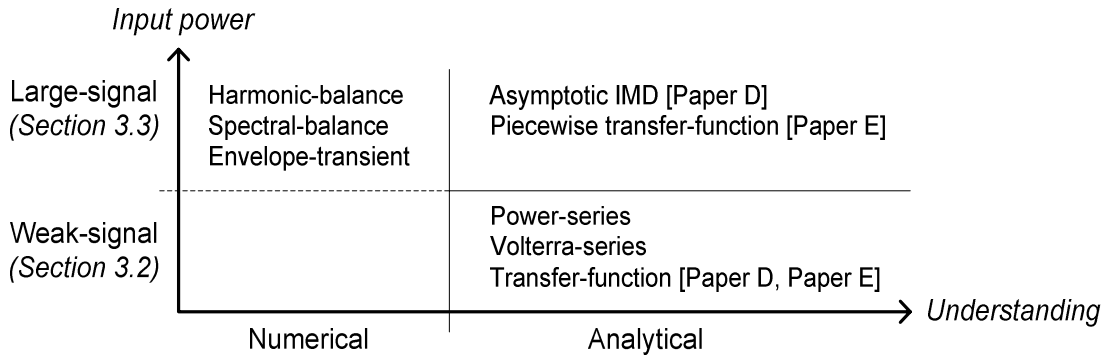

Fig. 3-7. Overview of PA IMD analysis methods treated.

3.2 Weak-signal IMD analysis

This section gives an introduction to commonly used weak-signal analysis methods. These use low-order Taylor-series expansions to approximate the device nonlinearities. This allows an analytical treatment of the PA IMD behavior by power-series analysis for memoryless nonlinearities or by Volterra-series analysis in the general case.

The weak-signal analyses are valid as long as the load-line does not traverse any strong nonlinearity, such as the turn-on or compression regions. The number of terms required for the Taylor series to be reasonably accurate would then rapidly increase (and eventually diverge) turning these analyses inefficient. For illustration, Taylor series with three terms will be used in this section.

3.2.1 Power series

If the IMD components generated are not fed back to the nonlinearity inputs, a *straightforward* power-series analysis may be used[1]. Fig. 3-8 shows a schematic of the PA in that case.

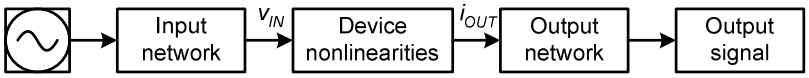

Fig. 3-8. The power amplifier described with a transfer-nonlinearity.

The device nonlinearity in Fig. 3-8 may be approximated by its third-order Taylor series,

$$i_{OUT}(v_{IN}) = I_{OUT,dc} + G_1 v_{IN} + G_2 v_{IN}^2 + G_3 v_{IN}^3 . \tag{3-1}$$

The coefficients G_n are proportional to the n'th order derivatives of the nonlinearity at the bias point.

It may be easily shown [41] that the generated IMD components in i_{OUT} are proportional to G_3,

$$\text{IMD} \propto G_3 |v_{IN}|^3 . \tag{3-2}$$

Note that the weak-signal IMD sign is therefore equal to the sign of G_3. The importance of the weak-signal IMD sign is discussed further in Section 3.3. Equation (3-2) also predicts the 3 dB/dB slope of weak-signal IMD versus input power as shown in Fig. 3-4.

3.2.2 Transfer function

For a FET PA, v_{IN} and i_{OUT} in Fig. 3-8 would be interpreted as v_{GS} and i_{DS}, respectively. However, straightforward power-series analysis may in general not be applied to FET PAs since the v_{DS} dependence of i_{DS} has been neglected. Feedback is caused by IMD components of i_{DS} being converted to IMD components in v_{DS} by the load-impedance.

[1] The special case with memoryless feedback is treated separately in Section 3.2.2.

The feedback may be considered as an internal node if a specific $V_{DS,bias}$ and load-impedance is considered. This allows the PA to be described by a new nonlinear transfer function (TF) $i_{OUT}(v_{IN})$. Hence, straightforward power-series analysis can again be used. It is still required that the feedback is memoryless. The load-impedance should therefore be purely resistive. Fig. 3-9 shows the resulting schematic of the PA circuit.

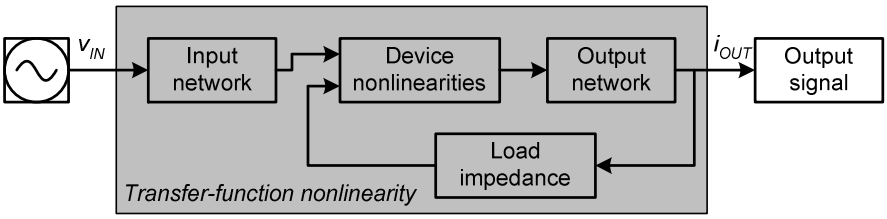

Fig. 3-9. Transfer function, $i_{OUT}(v_{IN})$, representation of the PA circuit when a specific load-impedance and $V_{DS,bias}$ is considered.

Carvalho and Pedro [42] used this method to analyze IMD in MESFET PAs. In [Paper D] and [Paper E] we applied the same method on LDMOS and CMOS PAs to study the influence of $V_{GS,bias}$ and input power on weak-signal PA IMD behavior.

The influence of the input- and output networks is small at low frequency, thus making $v_{IN} \approx v_{GS}$ and $i_{OUT} \approx i_{DS}$. The TF may then be approximated from the load-line, which determines the relation between i_{DS} and v_{GS} (*see* Fig. 3-2). It is generally impossible to find an explicit expression for the TF. In [Paper D] and [Paper E], the TF and its derivatives were obtained from harmonic-balance simulations with accurate large-signal transistor models (cf. Section 3.4).

Fig. 3-10 shows a typical TF and its derivatives, in this case obtained for a CMOS PA.

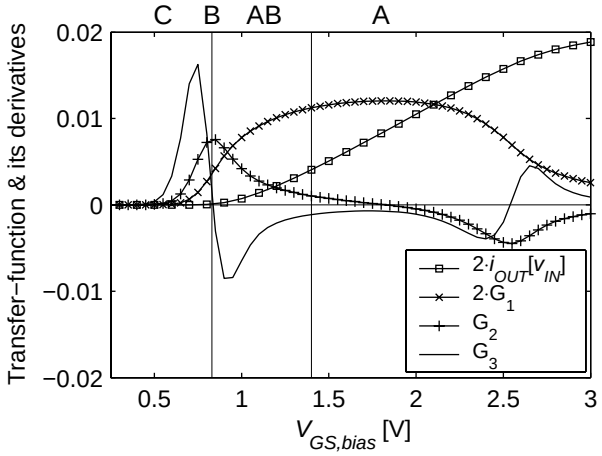

Fig. 3-10. Typical FET PA transfer function, $i_{OUT}(v_{IN})$, and its derivatives, G_n, versus gate-bias voltage. The corresponding classes of operation are indicated in top of the figure.

Equation (3-2) showed that weak-signal IMD is proportional to G_3. From Fig. 3-10, both the weak-signal IMD magnitude and sign is therefore seen to vary with $V_{GS,bias}$ for a CMOS PA. As an example, it is noted that G_3 is zero at $V_{GS,bias} \approx 0.8$ V. This

corresponds to a weak-signal sweet-spot that can give good IMD performance in small-signal amplifiers [Paper E]. This weak-signal sweet-spot is useless for PA applications since higher order contributions and large-signal effects will dominate the IMD behavior.

The TF representation has the advantage that it is valid for any input power level. In Section 3.3 it will be used to analyze the IMD behavior in large-signal operation where the signal excursion traverses the TF strong nonlinearities thus violating the assumptions for the other weak-signal analysis methods.

3.2.3 Volterra series

Volterra-series analysis, which is based on theories by Volterra [43], is a general method that can be used for circuits with both feedback and memory effects. It is therefore the most common method for general analytical IMD analysis. Fig. 3-11 shows the PA circuit in the general case.

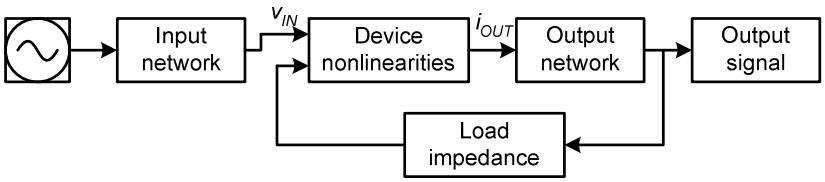

Fig. 3-11. The PA described as a nonlinear circuit with feedback.

For analyzing circuits with Volterra series, the *nonlinear-currents method* described in [41] is commonly used. The method is compatible with existing linear circuit analysis tools, and is based on a successive analysis of increasing orders of interaction (mixing orders) in the circuit. For every order, the nonlinear elements are successively replaced by corresponding *nonlinear-current* sources that depend on the Taylor-series expansion coefficients and lower-order voltages.

Pedro *et al.* [44] and Minasian [45] have used Volterra-series to investigate the influence of terminating impedances and device characteristics on small-signal FET amplifier IMD. It has also been used by Zhou and Kenney [46] and Pedro and Carvalho [40] to analyze IMD under wideband excitation.

Wambacq and Sansen [47] used Volterra series to develop symbolic circuit analysis tools. They used these methods to characterize the IMD behavior of common analog CMOS circuits in [48].

Although not suited for analyzing IMD in PAs under normal operating conditions, weak-signal Volterra- and power-series analysis are still the only methods available that allow an analytical treatment.

3.3 Large-signal IMD analysis

Large-signal methods need to be used for PA IMD prediction under normal operating conditions. Numerical methods are usually employed for this purpose.

First in this section commonly used numerical methods are reviewed. However, they do not reveal what mechanisms determine the IMD behavior obtained, but are useful as general circuit analysis tools for detailed IMD simulation. Alternative methods have rarely been reported.

The rest of this section therefore focuses on our work on analytical IMD analysis methods. These are approximate but allow the behavior of measured large-signal IMD behavior of PAs to be predicted and understood.

3.3.1 Numerical methods

Harmonic balance

Harmonic-balance analysis (HB) was first presented by Nakhla and Vlach [49]. HB is now the most commonly used numerical PA IMD analysis method and is implemented in most commercial CAE tools. Rizzoli and Neri review the development of the method in [50]. Recent developments are reported in [51].

The method is based on an iterative algorithm where the circuit is split in a linear- and a nonlinear network, and an initial voltage spectrum is guessed at the interface between those. The voltage spectrum is then iterated until the current spectral components match at the interface between the networks [41, 49].

The linear network is suited for calculations in frequency domain. There is, however, no general way to calculate the nonlinear current spectral components directly in frequency domain. The voltage spectrum must therefore first be converted to a time-domain waveform. This is used to calculate the nonlinear current waveform, which is finally converted back to frequency domain. Two discrete Fourier-transforms (DFTs) are needed in each iteration, which reduces the numerical precision and speed of the method, especially if several independent input frequencies are considered.

Spectral balance

Spectral-balance analysis (SB) is an iterative method closely related to HB, with the difference that the nonlinear current spectral components are calculated directly in frequency domain. The problems related to DFT can therefore be avoided.

A review of SB methods is given by Steer *et al.* in [52]. They also proposed the *arithmetic operator method* where the four basic arithmetic operators (+,–,×,÷) are represented by corresponding frequency domain operators [53]. A drawback is that the device models need to be reformulated with these operators. In [53], power series were used for the device model. Carvalho and Pedro [54] used Hermite rationals instead. They used SB to predict multi-tone IMD behavior in both weak- and large-signal regimes.

Närhi [55] described a related method where the bias dependent intrinsic *Y*-parameters are modeled by Chebyshev polynomials. This allowed the device strong nonlinearities to be better represented, which is important for large-signal IMD prediction.

Envelope transient

The input signal present in a real PA application is an up-converted stochastic base-band signal. This results in the base-band signal appearing as an envelope to the rapidly varying radio frequency (RF) carrier. Such signals can not be represented in frequency domain by a finite number of discrete frequencies. For IMD analysis with realistic input signals, the frequency domain methods above are therefore not suitable.

For this purpose, the envelope-transient analysis technique was presented by Ngoya and Larcheveque [56], Rizzoli *et al.* [57], and Sharrit [58], all within a short period of time.

The method combines HB analysis for the RF carrier with transient analysis for the discretized envelope. This results in a time evolving HB solution that can be interpreted in time- or frequency domain as desired.

The method can handle envelope memory, as well as, high frequency memory effects, but usually requires that the RF frequency is much higher than the base-band signal bandwidth.

3.3.2 Asymptotic IMD

Carvalho and Pedro [42] presented an IMD analysis method where conclusions about the weak-signal and asymptotic large-signal IMD signs are combined to predict different distinct IMD versus input power characteristics. In particular, they concluded that the large-signal IMD sweet-spots that had been reported for MESFETs [59] and LDMOS transistors [60] were due to change of sign in IMD between the weak- and large-signal input power regimes.

Consider, as an example, a PA operated in class C and described by the TF shown in Fig. 3-10. The weak-signal IMD will then be positive, due to the positive G_3 observed in class C.

On the other hand, the output power must saturate for sufficiently large input signal. As shown in Fig. 3-3, the measured output power is composed of an IMD part added to the linear response. The IMD must therefore become negative in saturation to compress the output power.

By combining these facts for the IMD sign in weak-signal and asymptotic large-signal operation, it is concluded that IMD must change sign at some power level for class C operation. This explains the appearance of a sweet-spot close to saturation in the CMOS class C measurements in Fig. 3-5.

A similar reasoning can be used for other modes of operation to predict different distinct IMD versus input power characteristics [42].

A similar method was used in [Paper D] to analyze LDMOS IMD behavior. However, the turn-on knee abruptness of LDMOS transistors compared to MESFETs made it necessary to revise the analysis in [42]. The resulting analysis method used is a special case of the one described below.

3.3.3 Piecewise transfer-function (PWTF)

This method was presented in [Paper E] and is based on approximating the TF representation of the PA by a piecewise function. This allows the large-signal IMD to be expressed analytically. Since the TF representation of the PA is used, it is assumed that $V_{DS,bias}$ and load impedance are fixed, and that reactive effects may be neglected.

The first order TF derivative, G_1, is approximated by a piecewise linear function as shown in Fig. 3-12.

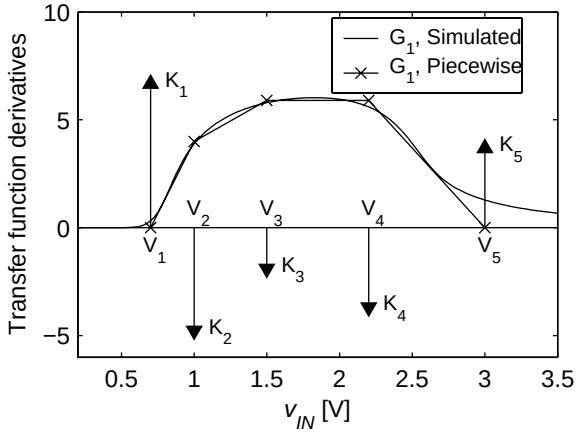

Fig. 3-12. Simulated first order transfer-function derivative, G_1, and a piecewise linear approximation of it. The corresponding third-order derivative is a set of Dirac-delta functions as indicated by arrows in the figure.

The piecewise G_1 approximation could be used to predict large-signal output power, but since that behavior is regular and easy to conceive, attention is on predicting IMD instead. The resulting third-order derivative, G_3, is considered for this purpose.

G_3 becomes a set of Dirac-delta functions (impulses) located at the piecewise linear G_1 breakpoints. The impulses have magnitudes equal to the change of slope in each of the G_1 breakpoints (*see* Fig. 3-12).

It can be shown [Paper E] that each of the G_3 impulses gives an individual IMD contribution depending on its magnitude, K_i, and voltage position, V_i, equal to:

$$\mathrm{IMD}_i \propto \frac{K_i \left(A^2 - \left(V_i - V_{GS,bias} \right)^2 \right)^{5/2}}{A^3} \tag{3-3}$$

where A is the input signal amplitude. Hence, the total IMD is found by adding the contributions from all impulses in G_3 that are traversed by the input signal excursion.

Only five breakpoints are used for the TF approximation in Fig. 3-12. This allows the mechanisms behind each of them to be interpreted as summarized in Table 3-1.

Table 3-1. Interpretation of the mechanisms behind the breakpoints in G_1.

G_1 breakpoint, i	*Device and PA mechanism*
#1	Turn-on; quadratic $i_{DS}(v_{GS})$ dependence at low currents
#2	Roll-off from quadratic towards linear dependence
#3	Quadratic to linear dependence
#4	i_{DS} compression when v_{DS} decreases along the load-line and approaches the triode region (*see* Fig. 3-2)
#5	i_{DS} saturation

Each of these breakpoints adds to the total IMD in i_{OUT} when they are traversed by the input signal. Fig. 2-7(a) illustrates how these contributions add to the total IMD when

the input signal amplitude, *A*, is swept and class AB operation is considered. Fig. 2-7(b) shows the total IMD in dB scale versus input power. Note the two IMD changes of sign (filled circles) in Fig. 2-7(a), and the corresponding two sweet-spots appearing in Fig. 2-7(b).

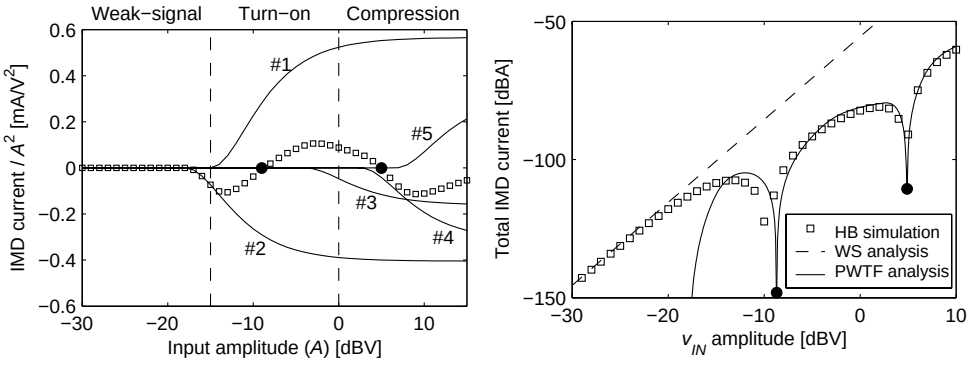

Fig. 3-13. Large-signal IMD predicted by the PWTF method for class AB operation. IMD sweet-spots are indicated with filled circles. a) The total IMD current (markers) and the individual contributions (numbered). Note that the vertical scale is normalized to the input amplitude squared. b) The total large-signal IMD current in dB-scale versus input power for class AB operation. Weak-signal (WS) and harmonic-balance (HB) simulation predictions are also shown.

The IMD behavior predicted by the PWTF method in Fig. 2-7(b) agrees well with the HB simulations and with the behavior of class AB measurements in Fig. 3-5. Evidently, only a few TF breakpoints are needed to predict complex large-signal IMD behavior well.

Since the breakpoints could be identified from fundamental PA and device mechanisms (Table 3-1), it is possible to use (3-3) and Fig. 2-7(a) to understand how they interact in creating the large-signal behavior measured.

Fig. 2-7(b) also illustrates that the PWTF analysis is a pure large-signal analysis. For weak-signal operation, when the input signal does not traverse any breakpoint, zero IMD is predicted. The analysis should thus be used together with a weak-signal analysis from Section 3.2 to predict the overall IMD versus input power behavior.

In combination, they can reproduce very well the behavior simulated with HB and an accurate transistor model. Methods for evaluating the accuracy of a transistor model for IMD analysis are described in Section 3.4.

3.3.4 Transfer-function measurement setup

The IMD analyses presented in our work are based on a TF representation of the PA. The TF has been determined using large-signal models and HB simulations. However, as high-frequency oscilloscopes are becoming available, the setup shown in Fig. 3-14 could eventually be used to measure it instead. It is important to note that the TF cannot be determined from dc measurements since the bias circuitry prevents any deviations in v_{GS} and v_{DS} from their bias voltages.

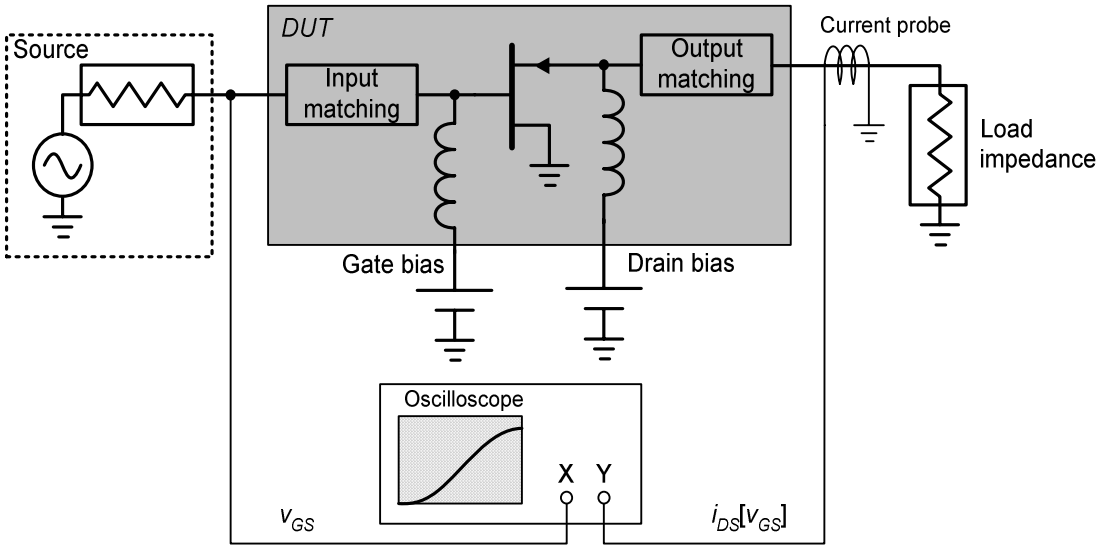

Fig. 3-14. Proposed setup for dynamically measuring the PA transfer-function.

The TF dependence of the load impedance could also be evaluated if a load-pull system is available. However, only resistive load-impedances may be used due to the assumptions of the TF representation.

A potential problem is that the measured TF may present hysteresis if reactive effects are present in the device or the terminating networks. At moderate excitation frequency, these effects are expected to have minor effect.

3.3.5 PWTF analysis applications

Turn-on knee analysis

Cripps [35] pointed out that the device turn-on characteristic to a large extent determines the large-signal IMD behavior of practical Class AB PAs. A numerical analysis was performed to study different turn-on knee characteristics. The same results could be obtained analytically using the PWTF analysis.

Device linearization

The influence of the turn-on region is seen in the appearance of the leftmost sweet-spot in Fig. 2-7. It can be shown, using the PWTF analysis, that it appears at an input power level which depends on $V_{GS,bias}$. Recently, there has been an interest to utilize this feature to create quasi-linear devices by combining several devices with slightly different turn-on voltages on the same chip. Thus, more sweet-spots will emerge that may be combined to create an overall favorable IMD behavior. Promising results are reported in [61].

Optimization of device characteristics

The PWTF analysis provides an analytical tool for finding the TF characteristic that results in a desired large-signal PA IMD behavior. The resulting TF gives information to device manufacturers on how their device characteristics should be tailored for optimal IMD performance in PA applications.

3.4 Large-signal models suitable for IMD prediction

The methods described in the previous sections can be used to understand measured IMD behavior. However, a detailed prediction of IMD normally requires numerical simulation with a large-signal transistor model.

Compared to the desired output signal, the IMD levels present in PAs are very low. Details in the device characteristics not detectable from *I*/*V*- and *S*-parameter measurements need therefore to be accurately modeled.

This section describes different methods used for extracting[2] large-signal FET models when accurate IMD prediction is desired. Methods to evaluate the ability of the models for IMD prediction in PA circuit applications are also discussed.

3.4.1 Extraction methods

Empirical models

Empirical large-signal models are usually based on multi-bias extraction of associated small-signal models. The bias dependencies of the extracted model parameters are then reproduced with suitable algebraic functions which form the large-signal model.

It is often desired to use a direct-extraction method [12] for the small-signal model parameter extraction. It is fast, reliable, and known to present well-behaved model parameter variations with bias [62]. The methods presented in Chapter 2 are well suited for this purpose since they allow optimal model parameter extractions to be performed for every bias point individually.

For other model topologies, not suited for direct-extraction, optimizer-based methods may be used. Niekerk *et al.* [63] presented a multi-bias extraction method that we have found very useful. They simultaneously optimize different bias-points versus measurements. The bias-dependent parameters are assigned independent values for every bias-point whereas the same values are used for the bias-independent parasitic element parameters. Their method is decomposition based, which means that the optimization it made on one parameter at a time in descending order depending on its relative influence on the global error. The sensitivity to the starting values and the risk of finding local minima is thereby minimized [64].

Empirical models have the advantage that they are based on measurements. Therefore, little prior knowledge of the device structure is needed, and the model can be extracted with the transistor mounted in the environment it is supposed to operate.

Physical models

Physical models take physical device properties, such as geometrical dimensions and doping levels, as input parameters and use physical relationships to derive the transistor characteristics. The models are usually scalable and therefore suitable for transistor-dense analog integrated circuit (IC) designs. So far, it is mainly used for MOSFETs and bipolar junction transistors (BJTs).

The BSIM3version3 from Berkeley University [65] and the MOS Model 11 from Philips [66] represent physical[3] MOSFET models that are commonly used within industry. Both models have almost 100 parameters. Normally, only the device manufacturer has enough knowledge to properly assign all model parameter values,

[2] The term *extraction* has a more general meaning here compared to Chapter 2.

[3] They both contain, to a certain extent, empirical expressions as well.

although measurement-based procedures for extracting some of the parameters are presented along with the model definition.

3.4.2 Verification of large-signal models

Before the large-signal models described above are used for predicting IMD in PAs, they should be verified for this purpose. Methods commonly used are described below.

Prediction of derivatives

It follows from the weak-signal analysis that a FET large-signal model needs to predict the i_{DS} derivatives well to be suited for weak-signal IMD analysis [67, 68]. The derivatives should if possible be extracted from measurements and compared to the ones obtained from differentiation of the model.

Maas and Crosmun [68] presented a method to extract the derivatives from measurements by only considering the v_{GS} dependence of i_{DS}. Pedro *et al.* [44] generalized this method to include both the v_{GS} and v_{DS} dependencies, where also the importance of including the v_{DS} dependence was stressed.

The principle is to apply, simultaneously, low frequency sinusoidal signals (10–100 MHz) to the gate- and drain device terminals. The harmonic and intermodulation power levels are then measured using a spectrum analyzer at the device output. Since the linear equivalent circuit is assumed known, it is possible to determine the complete set of i_{DS} derivatives.

We used this method in [Paper D] to measure the derivatives of an LDMOS transistor. A new large-signal model was also proposed. The results of the derivative measurement and model predictions are shown in Fig. 3-15.

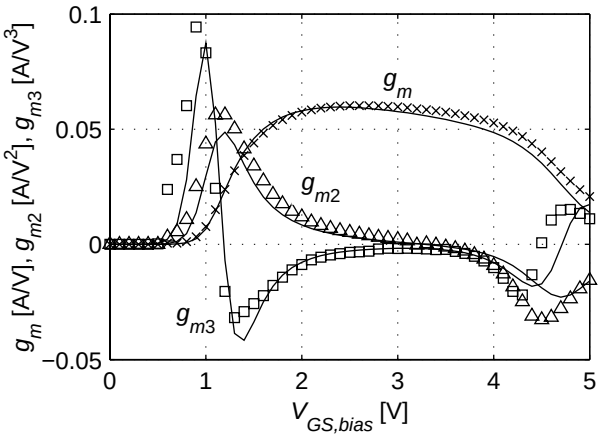

Fig. 3-15. Measured (markers) LDMOS i_{DS} derivatives versus gate bias voltage, $V_{GS,bias}$. Derivatives predicted by the model in [Paper D] are also shown (lines).

It is important that a large-signal model is built up from suitable functions that allow the higher order derivatives (especially g_{m3}) to be well represented for every bias-point. For MESFETs and HEMTs this is well known, and a good example, in this respect, is the HEMT model in [67]. There, g_{m3} (rather than i_{DS}) was modeled and the resulting expression integrated twice to give the desired i_{DS} model. Thereby, good weak-signal IMD prediction capabilities were guaranteed.

In [Paper D] it was shown that the industry-standard Motorola Electro-Thermal (MET) model [69] has a description of the turn-on knee that is not sharp enough to describe the LDMOS behavior. A modification to the model equations is proposed that result in improved IMD prediction capabilities.

[Paper E] evaluates the abilities of the CMOS BSIM3v3 model to reproduce measured derivatives. The model is shown to describe the derivatives and thus the weak-signal IMD behavior well for the tested device. A similar test is made for the MOS Model 11 in [70].

Power-spectrum measurements

Angelov *et al.* [71] have used power-spectrum measurements to validate their large-signal HEMT model [72, 73]. They applied a low frequency sinusoidal signal to the gate terminal and measured the harmonic content at the drain terminal. The measurements were made versus bias and input power and compared to simulations with their model. The description of strong nonlinearities can be verified if a large input signal is applied.

Two-tone measurements

The most commonly used method for evaluating large-signal models for PA applications is to perform two-tone measurements where the input power level is swept (*see* Fig. 3-5). Compared to the derivative extraction methods, which are made at low input power, two-tone measurements can be used to evaluate the description of the strong nonlinearities. The accuracy of the i_{DS} current model can be evaluated if the measurement is performed at low frequency. This was used to evaluate our LDMOS large-signal model in [Paper D] and the BSIM3v3 model in [Paper E].

Clark *et al.* [74] used two-tone measurements to develop a black-box behavioral PA model. Ku *et al.* [39] swept the two-tone spacing to study PA memory effects.

Two-tone measurements have limited value for device model extraction, since the results depend on the PA load impedance and excitation frequency used.

3.5 Conclusions

This chapter has concentrated on analytical IMD analysis methods. The results of these methods give insight in the mechanisms for generating the IMD behavior observed in practical PAs. These IMD analysis methods can be used in combination with existing methods for analyzing output power and efficiency to determine an initial compromise between them as required in PA designs.

Final optimization of the PA performance requires numerical simulation with accurate large-signal transistor models. The commonly used numerical simulation methods have been reviewed. Methods to evaluate the accuracy of large-signal transistor models for IMD prediction have also been covered.

FET PAs have been considered in this chapter. However, most presented methods are general an applicable to PAs with other devices.

Chapter 4. FMCW radar transceivers

As integrated of microwave circuits have become commercially available, a mass-market for low cost, short-range radars has emerged. Applications where those radars are used include automotive cruise control, automotive collision avoidance, door openers, and fluid level sensors. Since the operating frequency is very high in some of these systems, special care must be taken to select a radar principle and circuit solution that is easily integrated in MMIC technology. This is necessary to keep the cost of the radar at a minimum. For this reason, most of these radars are built using the frequency modulated continuous waveform (FMCW) radar technique. In contrast to pulsed radars, in which short pulses with high power are transmitted [75], these radars transmit and receive a signal at low but continuous power. FMCW radars can therefore use simpler solid-state transmitters since the demands on the power handling capability of the transmitter are set by the peak power.

In this chapter, the FMCW radar principle is described and common transceiver topologies discussed. Finally two FMCW radar transceivers suitable for MMIC integration [Paper F] and [Paper G] are presented.

4.1 Principle of operation

FMCW radars can be used to measure the range to and velocity of objects in front of the radar. To enable these measurements, the transmitted (TX) signal properties must be varied in time [75-77]. This is done by frequency modulation (FM) of the TX signal. For short-range radars, the frequency is most often swept triangularly versus time. The information about the object in front of the radar is then extracted from the difference between the TX frequency (f_{TX}) and received (RX) signal frequency (f_{RX}). A simple FMCW radar transceiver can then be realized as shown in Fig. 4-1, where the RX to TX frequency difference signal is found at the intermediate frequency (IF) port of the mixer.

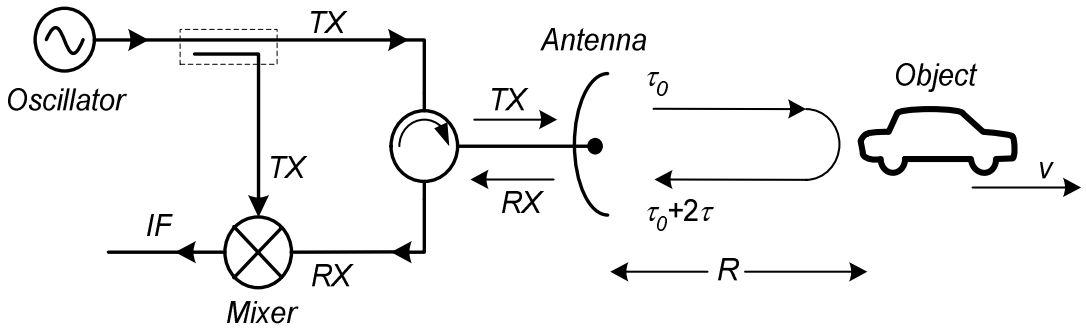

Fig. 4-1. Simple FMCW radar transceiver principle.

First, the object in front of the radar is assumed to not move relative to the radar, i.e. $v = 0$. Fig. 4-2 then shows the frequency of the different signals appearing in the transceiver versus time when a triangular FM is applied.

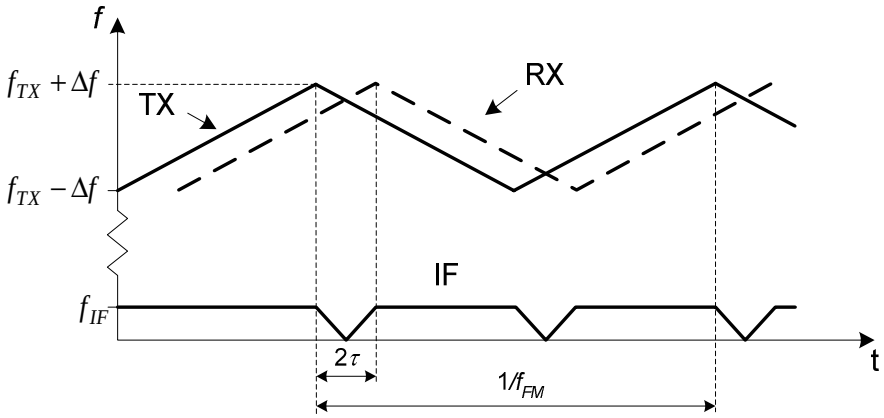

Fig. 4-2. Triangular frequency sweep for distance measurements in FMCW radars.

Since the TX wave has to travel to the object and back to the receiver, the RX frequency waveform will be delayed by the total round-trip time, 2τ.

Starting by studying the FM phase where f_{TX} is increasing, the frequency increase rate is equal to

$$\rho_{FM} = \frac{2\Delta f}{1/(2 f_{FM})} = 4\Delta f \cdot f_{FM} \tag{4-1}$$

The delay caused by the round-trip time of the wave will then cause a frequency difference between RX and TX resulting in an IF frequency (f_{IF}) equal to

$$f_{IF} = 2\tau \cdot \rho_{FM} \tag{4-2}$$

Since f_{IF} can be measured and ρ_{FM} is known, round-trip time, 2τ, can be found. The distance to the object, R, is then given by

$$R = c_0 \cdot \tau = \frac{f_{IF} \cdot c_0}{8 \cdot \Delta f \cdot f_{FM}} \tag{4-3}$$

where c_o is the free-space speed of light.

For the other phase of the FM, where the slope is negative, the resulting f_{IF} will have opposite sign. However, in the simple transceiver in Fig. 4-1 positive and negative frequencies appear as equal at IF.

For the range detection to be unambiguous, the transmitted wave must return to the receiver within the same modulation cycle it was transmitted. This corresponds to

$$R_{max} = \frac{c_0}{2 f_M} \tag{4-4}$$

For short-range radars, the maximum range of the radar is usually set by the receiver noise floor.

The range uncertainty is mainly set by imperfections in the FM waveform. For linear modulation, the range uncertainty, δR, can be related to the maximum frequency deviation, δf, from the ideal triangular FM waveform as [76, 78]

$$\delta R = \frac{\delta f \cdot R}{2\Delta f} \tag{4-5}$$

Equation (4-5) shows that the range uncertainty is proportional to the range. Maximum uncertainty therefore occurs at the maximum range of the radar. Different techniques to improve the range uncertainty by sweep linearization have been proposed [79-81].

If the object in front of the radar no longer is static, but moves with a constant velocity, v, receding from the radar, the RX frequencies in Fig. 4-2 will be affected. Due to the Doppler effect, the frequency of the RX signal will be shifted proportional to the object's velocity. The frequency shift due to the Doppler effect (*Doppler shift*) in the case of FMCW radars has been derived in [76] and is shown to be approximately equal to

$$f_d = -2 f_{TX} \cdot v / c_0 \tag{4-6}$$

where f_{TX} is the frequency of the transmitted wave. The resulting frequencies in the transceiver are shown in Fig. 4-3 versus time.

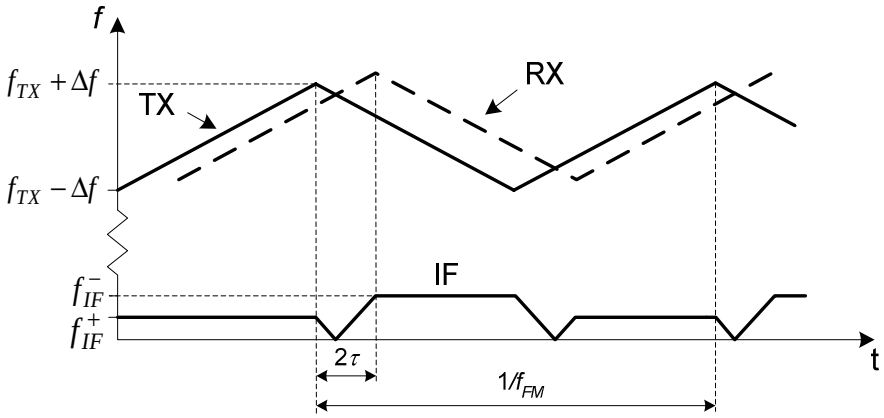

Fig. 4-3. Triangular frequency sweep in FMCW radars for distance and velocity measurements.

The total IF frequency will have contributions both from the round-trip time and from the *Doppler shift*. For the positive slope of the FM, the total frequency at IF is given by

$$f_{IF}^+ = f_{TX} - f_{RX} = f_{IF} - f_d = 2\tau \cdot \rho_{FM} + 2 f_{TX} \cdot v / c_0 \tag{4-7}$$

or, with the use of (4-1),

$$f_{IF}^+ = 8\tau \cdot \Delta f \cdot f_{FM} + 2 f_{TX} \cdot v / c_0 \tag{4-8}$$

Equation (4-8) depends on the instantaneous TX frequency, which varies as shown in Fig. 4-3. However, usually $\Delta f \ll f_{TX}$ and can therefore be considered unaffected by the FM.

For the negative slope phase of the FM, the corresponding frequency increase rate, ρ_{FM}, will be negative. This results in

$$f_{IF}^{-} = f_{TX} - f_{RX} = -f_{IF} - f_d = -8\tau \cdot \Delta f \cdot f_{FM} + 2 f_{TX} \cdot v / c_0 \tag{4-9}$$

or, since negative and positive frequencies can not be distinguished,

$$f_{IF}^{-} = 8\tau \cdot \Delta f \cdot f_{FM} - 2 f_{TX} \cdot v / c_0 \tag{4-10}$$

The object's distance can now be found by taking the average of f_{IF} over one modulation period, $\langle f_{IF} \rangle$, since

$$\langle f_{IF} \rangle = \frac{1}{2}\left(f_{IF}^{+} + f_{IF}^{-} \right) = 8\tau \cdot \Delta f \cdot f_{FM} \tag{4-11}$$

The distance to the object, *R*, is related to τ which yields,

$$R = c_0 \cdot \tau = \frac{\langle f_{IF} \rangle \cdot c_0}{8 \cdot \Delta f \cdot f_{FM}} \tag{4-12}$$

In a similar way, the object's velocity is found from the difference between the positive and negative slope IF frequencies,

$$\Delta f_{IF} = f_{IF}^{+} - f_{IF}^{-} = -4 f_{TX} \cdot v / c_0 \tag{4-13}$$

or

$$v = -\frac{c_0 \left(f_{IF}^{+} - f_{IF}^{-} \right)}{4 f_{TX}} \tag{4-14}$$

The maximum velocity that can be uniquely detected, is when the *Doppler shift* totally cancels the frequency shift caused by the round-trip time of the TX signal. In Fig. 4-3 this corresponds to $f_{IF}^{+} = 0$. The maximum velocity is then given by

$$v_{max} = \left| -\frac{4\tau \cdot \Delta f \cdot f_{FM} \cdot c_0}{f_{TX}} \right| = \frac{4R \cdot \Delta f \cdot f_{FM}}{f_{TX}} \tag{4-15}$$

4.2 Sources of noise

In FMCW radars, the transmitters and receivers are used simultaneously. Since the power level of the TX signal is much higher than the incident RX signal, leakage from TX to RX may saturate the receiver mixer and thus reduce the radar sensitivity. Furthermore, noise sidebands on the TX signal will be down-converted in the receiver leading to a decreased dynamic range [75-77, 79]. The down-conversion of noise sidebands to the TX signal in the receiver can be analyzed by separating the noise in amplitude modulation (AM) and FM noise contributions.

4.2.1 AM noise

Down-conversion of AM noise sidebands to the TX signal is generally the most severe problem. This effect can be reduced if a balanced mixer with good AM noise

suppression is used in the receiver [77, 82, 83]. However, there exists no way to prevent the AM noise sidebands from also appearing on the RX signal from being down-converted to IF in the receiver.

4.2.2 FM noise

For short-range radars, the correlation between the TX and RX signals is very strong. Therefore, when the TX signal is used to down-convert the RX signal (Fig. 4-1), the FM noise will be suppressed at IF [77, 83]. Because of this effect, the FM noise power at IF, S_{FM}, is proportional to

$$S_{FM} \propto \sin^2\left(\frac{2\pi \cdot R \cdot f_{FM}}{c_0}\right) \cong \left(\frac{2\pi \cdot R \cdot f_{FM}}{c_0}\right)^2 \qquad (4\text{-}16)$$

Since f_{IF} is proportional to the range, R, equation (4-16) shows that FM noise is substantially suppressed for short-range radars. As an example, a modulation rate, f_{FM}, of 1 kHz gives an FM noise suppression of 53 dB at 100 m due to this effect. TX oscillator FM noise is therefore often less severe than AM noise for short-range radars [77].

4.3 Transceiver topologies

As discussed in the previous section, good isolation from TX to RX is usually critical when designing FMCW radar transceivers.

A circulator is therefore often used, as shown in Fig. 4-1, to separate the transmitted and received signals [84-86]. The isolation obtained in circulators is typically 15-20 dB, but can be improved to 30-35 dB over a narrow frequency band [77]. The circulator can be built as a passive ferrite component or with active devices for integration in MMIC technology [87]. Also isolating hybrids and power dividers have been used for separation of transmitted and received signals [88, 89].

Even if the isolation in the circulator or hybrid is good, antenna port mismatch and reflections from objects close to the radar may cause an overall poor TX to RX isolation. The isolation can be improved by using an internal reference path, tuned to cancel these undesired reflections [90].

To further improve the TX to RX isolation, separate transmitter and receiver antennas can be used, as shown in Fig. 4-4 [91-93].

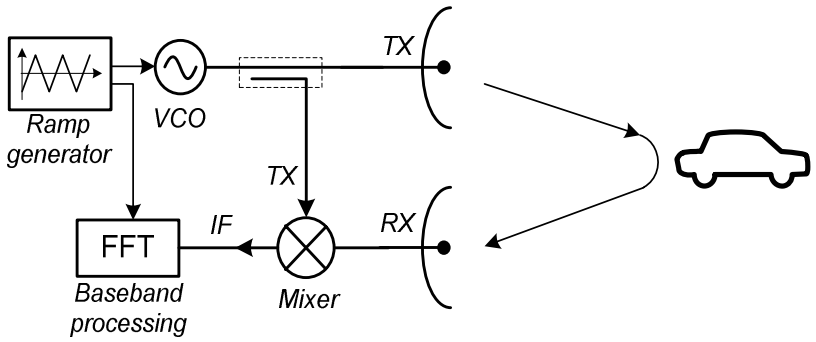

Fig. 4-4. Simple FMCW transceiver with separation of transmitted and received signals using individual antennas.

Separate antennas for transmission and reception can give an isolation of up to 60 dB [77]. However, this requires the antennas to be large and widely separated in order to create narrow beams and avoid electromagnetic interaction. Transceiver designs with separate TX and RX antennas become space consuming and therefore not suitable for high volume production in commercial applications.

A few transceiver topologies have also been proposed, where separation of transmitted and received signals is not needed [77, 94]. In [94] two diodes are used simultaneously for output power generation and down-conversion of the received signal making it attractive for integration in MMIC technology. However, since the MMIC processes are usually optimized for FETs, the diodes necessary for this design may be of poor quality.

As described above, separation of transmitted and received signals is a problem in most FMCW radar transceivers. In [Papers F] and [Paper G] two FET FMCW radar transceivers are presented which do not suffer from this problem.

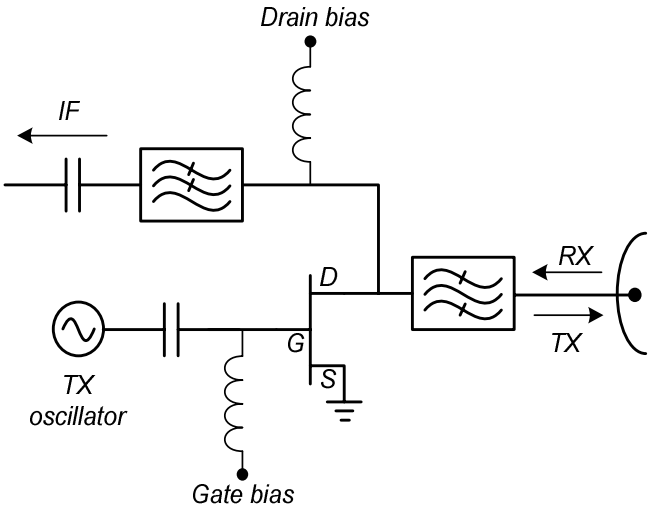

Fig. 4-5. FET FMCW radar transceiver.

Fig. 4-5 shows a schematic of the FET transceiver in [Paper F]. The FET is operated at intermediate bias voltages, where it is amplifying the TX oscillator signal and at the same time serves as a resistive FET mixer [95] for down-conversion of the RX signal. A detailed analysis of the FET transceiver has been made in [24].

As shown in Fig. 4-5, the FET transceiver has a very simple topology in which no separation is needed between the TX and RX signals. Lack of isolation between the TX and RX will appear as mismatch at the TX/RX port and is not likely to saturate the FET.

To improve the AM noise suppression properties of the FET transceiver in [Paper F], a balanced version of the transceiver is presented in [Paper G].

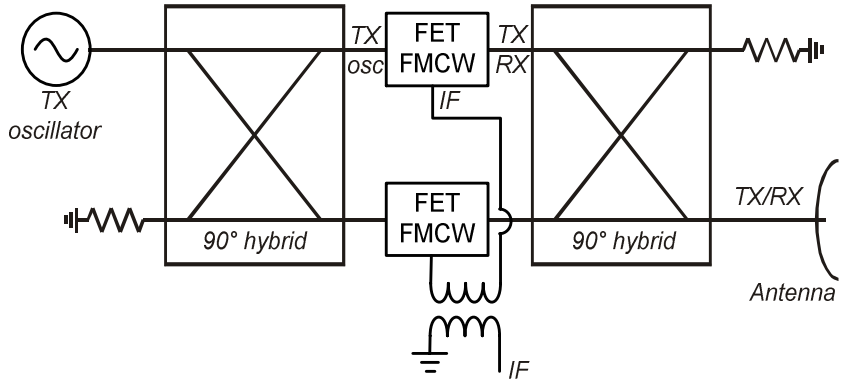

Fig. 4-6. Balanced FET FMCW radar transceiver.

The balanced transceiver consists of two unbalanced FET transceivers connected in a singly balanced quadrature hybrid configuration as shown in Fig. 4-6. This configuration suppresses down-conversion of AM noise in the TX oscillator to IF.

Both transceivers have been characterized in terms of output power, frequency response, AM noise suppression, and double sideband (DSB) noise performance [Paper G].

4.4 Conclusions

Two FET transceivers suitable for FMCW radars have been presented. The fact that no separation of the TX and RX signals is needed, their simple topology and that they are based on a FET devices make them suitable for integration in MMIC technology for commercial high volume applications.

Chapter 5. Summaries of appended papers

Seven papers are appended to the thesis (A–G). Papers A–C are related to FET model extraction whereas Paper D and Paper E treat the problem of predicting intermodulation in power amplifiers. Paper F and Paper G deal with a new FMCW radar transceiver topology.

5.1 Paper A

Optimal parameter extraction and uncertainty estimation in intrinsic FET small-signal models

The parameters of FET small-signal models are usually determined using the direct-extract method. In this paper we perform a theoretical uncertainty analysis of the model parameters obtained with that method. The analysis allows the derivation of model parameter uncertainties as a function of the *S*-parameter measurement uncertainties. Hence, an optimal extraction method is proposed where the model parameters are extracted with minimal uncertainty.

The model parameter uncertainties result in a corresponding uncertainty when the model is used for simulation. The uncertainty analysis is used also in the reverse direction to study the uncertainty in the modeled response.

5.2 Paper B

Statistical estimation of transistor small-signal model parameters

This paper is a generalization of the uncertainty analysis in [Paper A] where correlation between the *S*-parameter measurement uncertainties can be handled. This allows a very realistic representation to be used for the *S*-parameter measurement uncertainty. The uncertainty contributions from parasitic elements and measurement reference plane uncertainties are also investigated. These are shown to dominate the uncertainties in the estimated model parameters.

The presented estimation method is very general and thus applicable to parameter estimation for a variety of equivalent circuit models.

5.3 Paper C

A general de-embedding method

Paper C presents a general de-embedding method suited for FET modeling applications. The de-embedding equation is derived from a nodal-admittance matrix representation of the embedding (parasitic-element) network. Hence, the same de-embedding equation may be used independent of the parasitic-element topology. The method is exemplified on a standard FET parasitic element network. The results obtained allow the influence of the individual parasitic elements on the intrinsic FET

behavior to be studied. We have used these results for the uncertainty analysis in [Paper B].

5.4 Paper D

Prediction of IMD in LDMOS transistor amplifiers using a new large-signal model

In this paper we study the IMD behavior of LDMOS transistor PAs. Two-tone measurements are presented for different classes of operation. In particular we explained the origin of two very beneficial IMD minima appearing in class AB operation. An analysis is presented where it is shown that the sharp turn-on knee in LDMOS transistors may explain the appearance of these minima.

To accurately predict the measured IMD phenomena we also proposed a new large-signal model. The model is based on Motorola's industry-standard LDMOS model, but modified to predict IMD better.

5.5 Paper E

A comprehensive analysis of IMD behavior in RF CMOS power amplifiers

This paper presents a new large-signal IMD analysis method. It may be seen as a generalization of the method used to explain the LDMOS behavior in [Paper D]. The method allows the large-signal IMD to be regarded as a sum of individual contributions. Each contribution can be identified from the device characteristics, when operated along the PA load-line. We use this method to predict the large-signal IMD behavior of a CMOS PA circuit. The weak-signal IMD behavior and the ability of the industry-standard BSIM3v3 MOSFET model to predict measured performances for different classes of operation are also investigated.

5.6 Paper F

A FET transceiver suitable for FMCW radars

Paper F presents a new topology suitable for FMCW radar transceivers. We use a FET simultaneously as an amplifier for the transmitted signal and as a resistive mixer for the received signal. Hence the need for dual antennas, a circulator, or a coupler for the separation of the transmitted and received signals is obviated in FMCW radar applications. Measurements of a 10 GHz transceiver prototype are used to verify the principle. The transceiver's simple topology makes it suitable for commercial high-volume applications.

5.7 Paper G

A balanced FET FMCW radar transceiver with improved AM noise performance

AM noise is often limiting the performance of FMCW radars. In this paper we have improved the AM noise performance of the transceiver in [Paper F] by using a balanced topology. This resulted in 20 dB improvement in the AM noise performance compared with the unbalanced transceiver in [Paper F].

Acknowledgements

I would like to express my gratitude to the following persons and organizations who have helped me and supported my work:

First I would like to thank my supervisor Prof. Herbert Zirath for his support and encouragement during my studies.

Special thanks go to my co-supervisor Dr. Klas Yhland for guiding me in the right directions and without whose knowledge and skills mine would be far less.

I am obliged to Prof. José Carlos Pedro and Prof. Nuno Borges de Carvalho for making my six month stay at University of Averio, Portugal, a wonderful time and the beginning of a very inspiring collaboration.

Dr. Klas-Håkan Eklund for his enthusiasm and support.

Kristoffer Andersson, Assoc. Prof. Iltcho Angelov, Dr. Mikael Garcia, Assoc. Prof. Hans Hjelmgren, Tech. Lic. Lars Landén, Assoc. Prof. Peter Linnér, Dr. Niklas Rorsman, Assoc. Prof. Piotr Starski, and Dr. Jörgen Stenarson, for fruitful discussions and proofreading.

Magnus Andersson, Tech. Lic. Stefan Davidsson, Dr. Lars Dillner, Kristina Dynefors, Karine Enzel, Dr. Joakim Eriksson, Mattias Ferndahl, Naiara Goia, Tech. Lic. Marcus Hasselblad, Tech. Lic. Mattias Ingvarson, Dan Kuylenstierna, Anna Malmros, Tech. Lic. Anders Mellberg, Dr. Øistein Olsen, and Assoc. Prof. Jan Stake for interesting discussions about matters not always work related.

Dr. Jörgen Olsson, Dr. Lars Vestling, and Johan Ankarcrona at the Ångström Laboratory, Uppsala University, for fruitful cooperation within the LDMOS project.

The former staff at Gigatec AB, especially Christer Stoij and Kjell Jarl, for their support and interest in my work.

Assoc. Prof. Jan Grahn, Prof. Erik Kollberg, and Dr. Göran Lövestam for their management.

Jan Andersson, Lillemor Bergström, Catharina Forssén, Bente Larsson, Jan-Olof Lindgren, Anders Olausson, and Niklas Wadefalk for their administrative and technical support.

Everyone else at the Microwave Electronics Laboratory who has helped and encouraged me.

Chalmers Center for High Speed Technology (CHACH), the Swedish Foundation for Strategic Research (SSF), the Swedish Agency for Innovation Systems (VINNOVA), and Eklund Innovation for their financial support.

Finally, I would like to thank my friends and relatives for their patience and support during this work, and for giving me a life beyond Chalmers.

References

[1] A. Nordbotten, "LMDS systems and their application," *IEEE Communications Mag.*, vol. 38, pp. 150-4, Jun. 2000.

[2] M. Meehan and J. Purviance, *Yield and reliability in microwave circuit and system design*. Boston: Artech House, 1993.

[3] R. v. Nee and R. Prasad, *OFDM for wireless multimedia communications*. Boston: Artech House, 2000.

[4] J. Olsson, N. Rorsman, L. Vestling, C. Fager, J. Ankarcrona, *et al.*, "1 W/mm RF power density at 3.2 GHz for a dual-layer RESURF LDMOS transistor," *IEEE Electron Device Lett.*, vol. 23, pp. 206-8, Apr. 2002.

[5] R. Metzger, "LDMOS turns up the power," *Compound Semiconductor*, vol. 8, Jun. 2002.

[6] S. Mahdavi and A. A. Abidi, "Fully integrated 2.2-mW CMOS front end for a 900-MHz wireless receiver," *IEEE Journal of Solid-State Circuits*, vol. 37, pp. 662-9, May 2002.

[7] M. Steyaert, M. Borremans, J. Janssens, B. de Muer, I. Itoh, *et al.*, "A single-chip CMOS transceiver for DCS-1800 wireless communications," Proc. IEEE International Solid-State Circuits Conference, pp. 48-9, 411, 1998.

[8] M. Steyaert, J. Janssens, B. De Muer, M. Borremans, and N. Itoh, "A 2 V CMOS cellular transceiver front-end," Proc. IEEE International Solid-State Circuits Conference, pp. 142-3, 450, 2000.

[9] A. A. Abidi, "CMOS wireless transceivers: the new wave," *IEEE Communications Magazine*, vol. 37, pp. 119-24, Aug. 1999.

[10] H. H. Meinel, "Automotive radar and related traffic applications of millimeterwaves," Proc. 1997 Topical Symposium on Millimeter Waves, pp. 151-4, 1998.

[11] D. D. Si, S. C. Luo, C. Pero, W. Xiaodong, R. Knox, *et al.*, "Millimeter-wave FMCW/monopulse radar front-end for automotive applications," Proc. IEEE MTT-S Int. Microwave Symp., pp. 277-80, 1999.

[12] G. Dambrine, A. Cappy, F. Heliodore, and E. Playez, "A new method for determining the FET small-signal equivalent circuit," *IEEE Trans. Microwave Theory Tech.*, vol. 36, pp. 1151-9, Jul. 1988.

[13] M. Berroth and R. Bosch, "Broad-band determination of the FET small-signal equivalent circuit," *IEEE Trans. Microwave Theory Tech.*, vol. 38, pp. 891-5, July 1990.

[14] N. Rorsman, M. Garcia, C. Karlsson, and H. Zirath, "Accurate small-signal modeling of HFET`s for millimeter-wave applications," *IEEE Trans. Microwave Theory Tech.*, vol. 44, pp. 432-7, Mar. 1996.

[15] D. Lovelace, J. Costa, and N. Camilleri, "Extracting small-signal model parameters of silicon MOSFET transistors," Proc. IEEE MTT-S Int. Microwave Symp., pp. 865-8, 1994.

[16] R. A. Pucel, W. Struble, R. Hallgren, and U. L. Rohde, "A general noise de-embedding procedure for packaged two-port linear active devices," *IEEE Trans. Microwave Theory Tech.*, vol. 40, pp. 2013-24, Nov. 1992.

[17] L. O. Chua and P.-M. Lin, *Computer-aided analysis of electronic circuits : algorithms and computational techniques*. Englewood Cliffs, N.J.: Prentice-Hall, 1975.

[18] P. Walters, R. Pollard, J. Richardson, P. Gamand, and P. Suchet, "On-wafer measurement uncertainty for 3-terminal active millimetre-wave devices," Proc. IEEE GaAs IC Symp., pp. 55-8, 1992.

[19] R. Anholt and S. Swirhun, "Equivalent-circuit parameter extraction for cold GaAs MESFET's," *IEEE Trans. Microwave Theory Tech.*, vol. 39, pp. 1243-7, Jun. 1991.

[20] S. M. Kay, *Fundamentals of Statistical Signal Processing : Estimation Theory*: Prentice-Hall, 1993.

[21] J. W. Bandler, Z. Qi Jun, and R. M. Biernacki, "A unified theory for frequency-domain simulation and sensitivity analysis of linear and nonlinear circuits," *IEEE Trans. Microwave Theory Tech.*, vol. 36, pp. 1661-9, Dec. 1988.

[22] J. A. Rice, *Mathematical statistics and data analysis*, 2 ed. Belmont: Duxbury Press, 1993.

[23] D. F. Williams and R. B. Marks, "Comparison of on-wafer calibrations," Proc. 38th automatic RF technology group conf., pp. 68-81, 1991.

[24] K. Yhland, "Resistive FET mixers," Ph.D. Thesis, Chalmers University of Technology, Göteborg, Sweden, 1999

[25] R. W. Beatty, "2-port standards for evaluating automatic network parameter measurement systems," Proc. Conf. on Prec. Electromagnetic Measurements, 1974.

[26] "8510C Network Analyzer Data Sheet," Agilent Technologies 1999.

[27] *Agilent metrology forum*, Agilent Technologies, [Online] Available: http://metrologyforum.tm.agilent.com/download.shtml

[28] P. Sakalas, A. Mellberg, H. Zirath, N. Rorsman, and E. Choumas, "RF and microwave noise modeling of AlInAs/GaInAs/InP HFETs," Proc. 14th Indium Phosphide and Related Materials Conf., pp. 273-6, 2002.

[29] EA, "Expressions of the Uncertainty of Measurement in Calibration," European co-operation for Accreditation EA-4/02, 1999.

[30] R. Anholt, R. Worley, and R. Neidhard, "Statistical analysis of GaAs MESFET S-parameter equivalent-circuit models," *Int. J. Microwave and Millimeter-Wave Computer Aided Engineering*, vol. 1, pp. 263-70, Mar. 1991.

[31] J. Purviance, M. Meehan, and D. Collins, "Properties of FET parameter statistical data bases," Proc. IEEE MTT-S Int. Microwave Symp., pp. 567-70, 1990.

[32] J. W. Bandler, Q. J. Zhang, J. Song, and R. M. Biernacki, "FAST gradient based yield optimization of nonlinear circuits," *IEEE Trans. Microwave Theory Tech.*, vol. 38, pp. 1701-10, Nov. 1990.

[33] P. Banelli, G. Baruffa, and S. Cacopardi, "Effects of HPA non linearity on frequency multiplexed OFDM signals," *IEEE Trans. on Broadcasting*, vol. 47, pp. 123-36, Jun. 2001.

[34] E. Costa, M. Midrio, and S. Pupolin, "Impact of amplifier nonlinearities on OFDM transmission system performance," *IEEE Communications Lett.*, vol. 3, pp. 37-9, Feb. 1999.
[35] S. C. Cripps, *Advanced techniques in RF power amplifier design*. Boston: Artech House, 2002.
[36] S. C. Cripps, *RF power amplifiers for wireless communications*. Boston: Artech House, 1999.
[37] E. Ballesteros, F. Pérez, and J. Perez, "Analysis and design of microwave linearized amplifiers using active feedback," *IEEE Trans. Microwave Theory Tech.*, vol. 36, pp. 499-504, Mar. 1988.
[38] N. B. Carvalho and J. C. Pedro, "A comprehensive explanation of distortion sideband asymmetries," *IEEE Trans. Microwave Theory Tech.*, vol. 50, pp. 2090-2101, Sept. 2002.
[39] H. Ku, M. D. McKinley, and J. S. Kenney, "Quantifying memory effects in RF power amplifiers," *IEEE Trans. Microwave Theory Tech.*, vol. 50, pp. 2843-9, Dec. 2002.
[40] J. C. Pedro and N. B. Carvalho, "On the use of multitone techniques for assessing RF components' intermodulation distortion," *IEEE Trans. Microwave Theory Tech.*, vol. 47, Dec. 1999.
[41] S. A. Maas, *Nonlinear microwave circuits*. Norwood, MA: Artech House, 1988.
[42] N. B. Carvalho and J. C. Pedro, "Large- and small-signal IMD behavior of microwave power amplifiers," *IEEE Trans. Microwave Theory Tech.*, vol. 47, pp. 2364-74, Dec. 1999.
[43] V. Volterra and E. Whittaker, *Theory of functionals and of integral and integro-differential equations*. New York: Dover, 1959.
[44] J. C. Pedro and J. Perez, "Accurate simulation of GaAs MESFET's intermodulation distortion using a new drain-source current model," *IEEE Trans. Microwave Theory Tech.*, vol. 42, pp. 25-33, Jan. 1994.
[45] R. A. Minasian, "Intermodulation distortion analysis of MESFET amplifiers using the Volterra series representation," *IEEE Trans. Microwave Theory Tech.*, vol. 28, Jan. 1980.
[46] G. T. Zhou and J. S. Kenney, "Predicting spectral regrowth of nonlinear power amplifiers," *IEEE Trans. Communications*, vol. 50, pp. 718-22, May 2002.
[47] P. Wambacq and W. Sansen, *Distortion Analysis of Analog Integrated Circuits*: Kluwer Academic Publishers, 1998.
[48] P. Wambacq, G. G. E. Gielen, P. R. Kinget, and W. Sansen, "High-frequency distortion analysis of analog integrated circuits," *IEEE Trans Circuits and Systems II: Analog and Digital Signal Proc.*, vol. 46, pp. 335-45, Mar. 1999.
[49] M. S. Nakhla and J. Vlach, "A piecewise harmonic balance technique for determination of periodic response of nonlinear systems," *IEEE Trans. Circuits and Systems*, vol. 23, pp. 85-91, Feb. 1976.
[50] V. Rizzoli and A. Neri, "State of the art and present trends in nonlinear microwave CAD techniques," *IEEE Trans. Microwave Theory Tech.*, vol. 36, pp. 343-65, Feb. 1988.
[51] K. S. Kundert, "Introduction to RF simulation and its applications," *IEEE J. Solid-State circuits*, vol. 34, pp. 1298-319, Sept. 1999.

[52] M. B. Steer, C. R. Chang, and G. W. Rhyne, "Computer-Aided Analysis of Nonlinear Microwave Circuits Using Frequency-Domain Nonlinear-Analysis Techniques - the State-of- the-Art," *Int. J. Microwave and Millimeter-Wave Computer-Aided Engineering*, vol. 1, pp. 181-200, Feb. 1991.

[53] C. R. Chang and M. B. Steer, "Frequency-domain nonlinear microwave circuit simulation using the arithmetic operator method," *IEEE Trans. Microwave Theory Tech.*, vol. 38, pp. 1139-43, Aug. 1990.

[54] N. B. Carvalho and J. C. Pedro, "Multitone frequency-domain simulation of nonlinear circuits in large- and small-signal regimes," *IEEE Trans. Microwave Theory Tech.*, vol. 46, pp. 2016-2024, Dec. 1998.

[55] T. Närhi, "Frequency-domain analysis of strongly nonlinear circuits using a consistent large-signal model," *IEEE Trans. Microwave Theory Tech.*, vol. 44, pp. 182-92, Feb. 1996.

[56] E. Ngoya and R. Larcheveque, "Envelop transient analysis: a new method for the transient and steady state analysis of microwave communication circuits and systems," Proc. IEEE MTT-S Int. Microwave Symp., pp. 1365-8, 1996.

[57] V. Rizzoli, A. Neri, and F. Mastri, "A modulation-oriented piecewise harmonic-balance technique suitable for transient analysis and digitally modulated signals," Proc. 26th European Microwave Conf., 1996.

[58] D. Sharrit, "New method of analysis of communication systems," Proc. IEEE MTT-S nonlinear CAD workshop, 1996.

[59] C. C. Blanco, "Gain expansion and intermodulation in a MESFET amplifier," *Electronics Letters*, vol. 15, pp. 31-2, July 1979.

[60] S. R. Novis and L. Pelletier, "IMD parameters describe LDMOS device performance," *Microwaves & RF*, vol. 37, pp. 69-74, July 1998.

[61] D. R. Webster, G. Ataei, and D. G. Haigh, "Low-distortion MMIC power amplifier using a new form of derivative superposition," *IEEE Trans. Microwave Theory Tech.*, vol. 49, pp. 328-32, Feb. 2001.

[62] M. Garcia, K. Yhland, H. Zirath, I. Angelov, and N. Rorsman, "Fast, automatic and accurate HFET small-signal characterization," *Microwave Journal*, vol. 40, pp. 102-17, Jul. 1997.

[63] C. van Niekerk, P. Meyer, D. M. M.-P. Schreurs, and P. B. Winson, "A robust integrated multibias parameter-extraction method for MESFET and HEMT models," *IEEE Trans. Microwave Theory Tech.*, vol. 48, pp. 777-86, May. 2000.

[64] C. van Niekerk and P. Meyer, "Performance and limitations of decomposition-based parameter extraction procedures for FET small-signal models," *IEEE Trans. Microwave Theory Tech.*, vol. 46, pp. 1620-7, Nov. 1998.

[65] W. Liu, X. Jin, J. Chen, M.-C. Jeng, Z. Liu, *et al.*, *BSIM3v3.2.2 MOSFET Model: Users' Manual*. University of California, Berkeley, 1999.

[66] *Philips MOS Model 11*, Philips Semiconductors, [Online] Available: http://www.semiconductors.philips.com/Philips_Models/

[67] S. Peng, P. J. McCleer, and G. I. Haddad, "Nonlinear models for the intermodulation analysis of FET mixers," *IEEE Trans. Microwave Theory Tech.*, vol. 43, pp. 1037-45, May 1995.

[68] S. A. Maas and A. Crosmun, "Modeling the gate I/V characteristic of a GaAs MESFET for Volterra-series analysis," *IEEE Trans. Microwave Theory Tech.*, vol. 37, pp. 1134-6, Jul. 1989.

[69] W. R. Curtice, J. A. Pla, D. Bridges, T. Liang, and E. E. Shumate, "A new dynamic electro-thermal nonlinear model for silicon RF LDMOS FETs," Proc. IEEE MTT-S Int. Microwave Symp., pp. 419-22, 1999.

[70] R. van Langevelde, L. F. Tiemeijer, R. J. Havens, M. J. Knitel, R. F. M. Roes, *et al.*, "RF-distortion in deep-submicron CMOS technologies," Proc. IEDM, Electron Device Meeting, pp. 807-810, 2000.

[71] I. Angelov, H. Zirath, and N. Rorsman, "Validation of a nonlinear transistor model by power spectrum characteristics of HEMTs and MESFETs," *IEEE Trans. Microwave Theory Tech.*, vol. 43, pp. 1046-1052, May 1995.

[72] I. Angelov, L. Bengtsson, and M. Garcia, "Extensions of the Chalmers nonlinear HEMT and MESFET model," *IEEE Trans. Microwave Theory Tech.*, vol. 44, pp. 1664-74, Oct. 1996.

[73] I. Angelov, H. Zirath, and N. Rorsman, "A new empirical nonlinear model for HEMT and MESFET devices," *IEEE Trans. Microwave Theory Tech.*, vol. 40, pp. 2258-66, Dec. 1992.

[74] C. J. Clark, C. P. Silva, A. A. Moulthrop, and M. S. Muha, "Power-amplifier characterization using a two-tone measurement technique," *IEEE Trans. Microwave Theory Tech.*, vol. 50, pp. 1590-602, Jun. 2002.

[75] M. I. Skolnik, *Introduction to radar systems*, 2 ed. New York: McGraw-Hill, 1980.

[76] J. L. Eaves and E. K. Reedy, "Principles of modern radar." New York: Van Nostrand Reinhold, 1987, pp. 405-7.

[77] A. G. Stove, "Linear FMCW radar techniques," *IEE Proceedings F (Radar and Signal Processing)*, vol. 139, pp. 343-50, 5 1992.

[78] S. O. Piper, "Receiver frequency resolution for range resolution in homodyne FMCW radar," Proc. 1993 IEEE National Telesystems Conference, pp. 169-73, 1993.

[79] H. D. Griffiths, "New ideas in FM radar," *Electronics & Communication Engineering Journal*, vol. 2, pp. 185-94, 5 1990.

[80] T. Musch, N. Rolfes, and B. Schiek, "A highly linear frequency ramp generator based on a fractional divider phase-locked-loop," *IEEE Trans. Instrumentation and Measurement*, vol. 48, pp. 634-7, 2 1999.

[81] J. Fuchs, K. D. Ward, M. P. Tulin, R. A. York, and R. G. Ranson, "Simple techniques to correct for VCO nonlinearities in short range FMCW radars," Proc. IEEE MTT-S Int. Microwave Symp., pp. 1175-8, 1996.

[82] S. A. Maas, *Microwave mixers*, 2 ed. Boston: Artech House, 1993.

[83] M. I. Skolnik, *Radar handbook*. New York: McGraw-Hill, 1970.

[84] S. F. Paik and L. Kirby, "MMIC radar transceivers for industrial sensors," Proc. IEEE MTT-S Int. Microwave Symp., pp. 1063-5, 1995.

[85] D. Brumbi and T. Perkins, "Low power FMCW radar system for level gaging," Proc. IEEE MTT-S International Microwave Symposium, pp. 1559-62, 2000.

[86] C. Jing, X. Yang, Z. Feng, and Y. zhang, "A front-end of FMCW anticollision radar," Proc. Int. Conf. Microwave and Millimeter Wave Tech., pp. 568-71, 2000.

[87] P. Katzin, Y. Ayasli, L. Reynolds, Jr., and B. Bedard, "6 to 18 GHz MMIC circulators," *Microwave Journal*, vol. 35, pp. 248-56, 5 1992.

[88] J. Kehrbeck, E. Heidrich, and W. Wiesbeck, "A novel and inexpensive short range FM-CW radar design," Proc. International Conference Radar 92, pp. 288-91, 1992.

[89] M. Nalezinski, M. Vossiek, P. Heide, and G. A. Koepf, "Novel 24 GHz FMCW front-end with 2.45 GHz SAW reference path for high-precision distance measurements," Proc. IEEE MTT-S Int. Microwave Symp., pp. 185-8, 1997.

[90] P. D. L. Beasley, A. G. Stove, B. J. Reits, and B. As, "Solving the problems of a single antenna frequency modulated CW radar," Proc. IEEE 1990 International Radar Conference, pp. 391-5, 1990.

[91] K. W. Chang, G. S. Dow, H. Wang, T. N. Chen, K. Tan, *et al.*, "A W-band single-chip transceiver for FMCW radar," Proc. IEEE 1993 Microwave and Millimeter-Wave Monolithic Circuits Symp., pp. 41-4, 1993.

[92] R. J. Kenefic, "Performance of an FMCW radar sensor," *IEEE Trans. Communications*, vol. 40, pp. 1675-8, 11 1992.

[93] J. E. Muller, T. Grave, H. J. Siweris, M. Karner, A. Schafer, *et al.*, "A GaAs HEMT MMIC chip set for automotive radar systems fabricated by optical stepper lithography," *IEEE J. Solid State Circuits*, vol. 32, pp. 1342-9, 9 1997.

[94] S. A. Maas, "FM-CW radar transceiver," U. S. Patent 5 596 325, Jan. 21, 1997.

[95] S. A. Maas, "A GaAs MESFET mixer with very low intermodulation," *IEEE Trans. Microwave Theory Tech.*, pp. 425-9, Apr. 1987.